Nano-Micro Letters

e-ISSN 2150-5551
CN 31-2103/TB

ARTICLE

https://doi.org/10.1007/s40820-026-02151-6



**Cite as**
Nano-Micro Lett.
(2026) 18:304

Received: 22 November 2025
Accepted: 2 March 2026


# Crystalline $Ni_3S_2$ Nanorods Tuned by Low-Crystalline $NiCoS_x$ with Built-In Electric Field for Efficient Overall Water Splitting

Neng Chen[1], Jun He[1], Hongqiang Li[1], Dedong Jia[1], Haoran Qian[1], Huan Pang[2] ✉, Jieshan Qiu[3] ✉, Yongfeng Li[4], Xiaojun He[1] ✉

## HIGHLIGHTS

- Low-crystalline $NiCoS_x$-armored $Ni_3S_2$ nanorod heterostructure inhibits sulfide loss.
- Built-in electric field effect induced by work function accelerates electron transfer.
- The $NiCoS_x$@$Ni_3S_2$/NF exhibits superior hydrogen and oxygen evolution reactions activity and stability.

**ABSTRACT** Efficient overall water splitting (OWS) technology has been highly demanded across the world, of which the key is the development of active and stable electrocatalysts for both hydrogen and oxygen evolution reactions (HER/OER). Herein, novel crystalline $Ni_3S_2$ nanorods tuned by low-crystalline $NiCoS_x$ ($NiCoS_x$@$Ni_3S_2$) are synthesized via an ion-exchange strategy. The built-in electric field at the heterogeneous interface driven by work function difference, facilitates rapid electron transfer from $Ni_3S_2$ to $NiCoS_x$ via a robust Ni–S–Co bond bridge. This synergistic combination of the conductive crystalline core and low-crystalline shell optimizes the d-band center, balancing intermediate adsorption/desorption, speeding up water dissociation, enhancing hydrogen adsorption/desorption for HER, and lowering the energy barrier for OER, ultimately boosting OWS efficiency. The defect-rich, low-crystalline NiCoS*x* shell, bonded to the crystalline core via Ni–S–Co bonds, serves as a protective armor, enabling dynamic reconstruction into NiCoOOH and suppresses sulfide leaching, ensuring catalytic stability. The optimized $NiCoS_x$@$Ni_3S_2$ achieves low HER/OER overpotentials of 346/520 mV@1000 mA $cm^{-2}$, evidenced by an ultralow cell voltage of 2.10 V@1000 mA $cm^{-2}$ for OWS and long-term durability up to 400 h. The work paves a novel way to fabricate sulfur-based electrocatalysts with high yet balanced activity and stability for OWS via an interface engineering strategy.

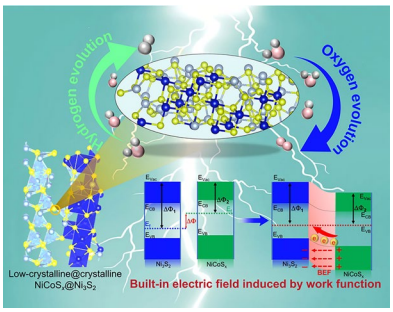


**KEYWORDS** $NiCoS_x$@$Ni_3S_2$; Low-crystalline tuned crystalline heterostructure; Built-in electric field; Work function; Water splitting

✉ Huan Pang, panghuan@yzu.edu.cn; Jieshan Qiu, qiujs@mail.buct.edu.cn; Xiaojun He, xjhe@ahut.edu.cn
[1] School of Chemistry and Chemical Engineering, Anhui Province Key Laboratory of Coal Clean Conversion and Low Carbon Utilization, Anhui Province Key Laboratory of Efficient Conversion and Solid-State Storage of Hydrogen & Electricity, Key Laboratory of Metallurgical Emission Reduction and Resources Recycling, Ministry of Education, Anhui University of Technology, Ma'anshan, Anhui 243002, People's Republic of China
[2] Institute of Innovation Materials and Energy, School of Chemistry and Chemical Engineering, Yangzhou University, Yangzhou 225002, People's Republic of China
[3] College of Chemical Engineering, State Key Laboratory of Chemical Resource Engineering, Beijing University of Chemical Technology, Beijing 100029, People's Republic of China
[4] State Key Laboratory of Heavy Oil Processing, China University of Petroleum, Beijing 102249, People's Republic of China

Published online: 26 March 2026

## 1 Introduction

Hydrogen has emerged as one of the most promising clean energy carriers, providing a sustainable alternative to conventional fossil fuels due to its exceptional energy density and zero-carbon emissions in the global transition to a low-carbon economy [1, 2]. Electrochemical overall water splitting (OWS), which involves hydrogen evolution reaction (HER) and oxygen evolution reaction (OER), is considered one of the most promising technologies for efficient and sustainable hydrogen production [3, 4]. However, the large-scale industrial application of OWS is hampered by inherent limitations of state-of-the-art transition metal-based electrocatalysts including industrial-grade current densities, overpotential surges drastically due to insufficient active sites, sluggish mass/charge transfer, and mismatched intermediate adsorption energies [5, 6]. Harsh oxidative/reductive electrolytic environments trigger active phase exfoliation, lattice strain, and surface corrosion, with even cutting-edge catalysts barely stable for over 100 h at 1000 mA $cm^{-2}$. Cost-efficiency is compromised by high cost/scarcity of noble metals and the complex synthesis process/poor stability of non-noble transition metal-based alternatives [7–9]. Therefore, it is urgent to develop transition metal-based electrocatalysts with balanced activity and stability for OWS [10, 11].

In the last few years, transition metal compounds, including transition metal oxides [12], phosphides [13], sulfides (TMSs) [14], nitrides [15], have undergone extensive research due to their availability and cost-efficiency. Among them, transition metal sulfides (TMSs, such as $M_3S_2$ and $M_9S_8$) exhibit excellent catalytic potential in HER and OER reactions, attributing to their unique d-electron configurations and adjustable sulfur coordination environments [16, 17]. Sulfur doping, in particular, is able to significantly modulate the electronic structure by adjusting electron density to optimize intermediate adsorption and charge transfer processes [18]. Sulfur doping or metal substitution can optimize the electronic structure and adjust the adsorption free energies of intermediates (H*, *OOH), thus enhancing catalytic activity [19, 20]. Furthermore, advanced interface engineering approaches, particularly the construction of well-designed heterostructures, have shown advantages in optimizing interfacial charge distribution and boosting catalytic performance [21, 22]. At present, it is necessary to establish a bi-directional regulation strategy in terms of $O_2$/$H_2$ intermediate binding energies to optimize the catalyst performance.

In recent years, low-crystallinity materials have gained widespread attention in the field of catalysis due to their atomic disorder, high density of dangling bonds, and abundant lattice defects. These structural features provide two core advantages for low-crystallinity materials: (1) high surface activity: amorphous/low-crystal surfaces expose more unsaturated coordination sites to optimize the adsorption of reaction intermediates; (2) excellent stability: disordered structures mitigate lattice strain at high potentials, preventing catalyst dissolution or phase transitions [23, 24]. Therefore, low-crystallinity materials are often regarded as a "low-crystal/amorphous skin" to offer more active sites and enhanced material stability [25, 26]. The long-range disorder of low-crystallinity materials leads to low charge carrier mobility, severely limiting electronic transport efficiency and thereby affecting catalytic kinetics [27, 28]. Yet, the conductivity of low-crystallinity materials is insufficient to support efficient catalysis. Thus, enhancing charge carrier mobility while maintaining surface activity remains a critical challenge.

To address this issue, researchers have proposed a gradient structural design strategy, wherein a long-range ordered crystalline framework (e.g., carbon coating or metal support) is constructed within the core of low-crystallinity materials to improve electronic conductivity, while the outer layer retains the high-activity defect structure, maintaining surface activity while enhancing conductivity [29, 30]. Despite progress in this area, the structural reconstruction of low-crystallinity/crystalline interfaces and the deactivation of active sites at high potentials and currents remain unresolved issues [31, 32]. Recent research has revealed that the built-in electric field (BEF) induced by the work function difference ($\Delta\Phi$-induced BEF) can significantly optimize catalytic behavior at high potentials and currents. $\Delta\Phi$-induced BEF drives charge redistribution at the interface, optimizing the adsorption of intermediates (such as $H_2$/$O_2$), thus improving catalytic efficiency [33, 34]. For example, Zhang et al. [35] utilized $\Delta\Phi$-induced BEF in the $Ni_3S_2$/$Co_3O_4$ heterostructure to enhance urea molecule adsorption, improving electrooxidation efficiency. BEF is used to modulate the hydrogen adsorption free energy in the $Ni_2P$–CoCH sulfide heterostructure, reducing the HER overpotentials [36]. However, most current studies focus on BEF mechanisms at crystalline heterojunctions, and the BEF formation mechanism at


https://doi.org/10.1007/s40820-026-02151-6

low-crystallinity/crystalline interfaces remains unclear [37, 38]. Moreover, at high potentials and currents, structural reconstruction and active site deactivation at low-crystallinity/crystalline interfaces have yet to be fully resolved [39–42]. Hence, it is a challenge to achieve engineering of low-crystalline/crystalline heterogeneous interface with ΔΦ-induced BEF to develop OWS electrocatalysts with high yet balanced activity and stability. In all, the scale-up of OWS technology for industrial applications is plagued by specific bottlenecks including performance decay at high current densities, poor durability in harsh electrolytic environments, and cost-effectiveness imbalance [43–45].

Herein, we report crystalline $Ni_3S_2$ nanorods tuned by low-crystalline $NiCoS_x$ ($NiCoS_x$@$Ni_3S_2$) by an anion and cation exchange strategy. The ultraviolet photoelectron spectroscopy (UPS) spectra, X-ray absorption near edge structure (XANES) spectra and density functional theory (DFT) calculations reveal that the ΔΦ-induced BEF at $NiCoS_x$/$Ni_3S_2$ heterogeneous interface facilitates electron transfer through Ni–S–Co interfacial bridge, enhancing water dissociation and optimizing hydrogen adsorption/desorption for HER. Meanwhile, the BEF in $NiCoS_x$@$Ni_3S_2$ reduces the reaction energy barrier of *O → *OOH for OER, thereby promoting the overall catalytic kinetics of water splitting. In situ Raman and X-ray photoelectron spectroscopy (XPS) characterization results illustrate that the ultra-thin $NiCoS_x$ layer functions as a protective armor to avoid or suppress the sulfide loss, resulting in high catalytic activity and stability of the $NiCoS_x$@$Ni_3S_2$ catalysts. The $NiCoS_x$@$Ni_3S_2$ with tuned structure makes the HER/OER possible at a low overpotential of 346/520 mV@1000 mA $cm^{-2}$, evidenced by an ultralow cell voltage of 2.10 V@1000 mA $cm^{-2}$ for OWS and long-term durability up to 400 h at current densities of 1000 mA $cm^{-2}$, outperforming most of the TMS-based electrocatalysts in literature. The work paves a way to fabricate sulfur-based electrocatalysts with high yet balanced activity and stability for OWS via interface engineering strategy.

## 2 Experimental Section

### 2.1 Synthesis of $Ni(OH)_2$/NF

To remove the oxide layer, Ni foam (NF, 2 cm × 2 cm) was sonicated in ethanol, acetone, and HCl solution for 15 min, respectively. Subsequently, the NF was soaked in deionized (DI) water at 80 °C for 3 h to grow $Ni(OH)_2$ nanosheets on NF surface. The resulting samples were repeatedly washed with ethanol and air-dried at room temperature. The sample was labeled as $Ni(OH)_2$/NF.

### 2.2 Synthesis of $NiCo_2O_4$@NiO/NF

To investigate the regulation effects of temperature and time on the cation exchange process, the as-prepared $Ni(OH)_2$/NF was immersed into 0.1 M $Co(NO_3)_2$ aqueous solution under different reaction conditions: varying temperatures (40, 80, 120, and 160 ˚C) for 3 h, and varying durations (0.5, 1, 3, and 6 h) at the temperature of 120 °C. After the cation exchange reaction, the sample was taken out and dried naturally at room temperature to form Ni/$Co(OH)_2$/NF nanosheet arrays. The as-prepared Ni/$Co(OH)_2$/NF was oxidized in a tube furnace under air atmosphere at 350 °C for 2 h to obtain $NiCo_2O_4$@NiO/NF nanosheets.

### 2.3 Synthesis of $NiCoS_x$@$Ni_3S_2$/NF

Analogous to the cation exchange regulation, the anion exchange sulfidation process was also optimized by adjusting temperature and time. Specifically, the as-prepared $NiCo_2O_4$@NiO/NF was vertically erected in 30 mL of 50 mmol $L^{-1}$ thiourea solution, and the mixture was transferred into a 100 mL Teflon-lined autoclave. The autoclave was sealed and maintained under different reaction conditions: varying temperatures (80, 120, 160, and 200 °C) with a fixed duration of 3 h, and varying durations (0.5, 1, 3, and 6 h) at a fixed temperature of 160 °C. After the anion exchange sulfidation reaction, the autoclave was naturally cooled to room temperature. The resulting electrode material was thoroughly washed with ethanol and DI water to remove unreacted thiourea and by-products, then dried naturally at room temperature. The final product, composed of crystalline $Ni_3S_2$ nanorods tuned by low-crystalline $NiCoS_x$, was denoted as $NiCoS_x$@$Ni_3S_2$/NF.

### 2.4 Synthesis of $Ni_3S_2$/NF and $NiCoS_x$/NF

$Ni_3S_2$/NF was synthesized by the same procedure with the absence of $Co(NO_3)_2$. $NiCoS_x$/NF was synthesized by the same procedure with the presence of $Ni(OH)_2$/NF in 0.1 M

$Co(NO_3)_2$ solution at 80 °C for 12 h for sufficient cation exchange and was oxidized in a tube furnace to obtain $NiCo_2O_4$/NF. The $NiCo_2O_4$/NF was etched using thiourea at 160 °C for 12 h for sufficient anion exchange.

## 3 Results and Discussion

### 3.1 Synthesis and Characterization of Low-Crystalline $NiCoS_x$-Tuned Crystalline $Ni_3S_2$

As illustrated in Fig. S1, the crystalline $Ni_3S_2$ nanorods tuned by low-crystalline $NiCoS_x$ were synthesized via three-step procedure, e.g., in situ growth, anion and cation exchange, in which nickel foam (NF) serves as the conductive substrate and nickel source. First, $Ni(OH)_2$/NF was prepared in situ on nickel foam at 80 °C in deionized water, where NF undergoes spontaneous surface oxidation, generating $Ni^{2+}$, $OH^-$, and hydrogen gas. This electrochemical corrosion process is shown as: $2Ni + 2H_2O + O_2 \rightarrow 2Ni(OH)_2$. When the $Ni^{2+}$ and $OH^-$ reach a high concentration near the NF surface, they form $Ni(OH)_2$ and deposit back onto the surface. Subsequently, Ni/$Co(OH)_2$/NF was formed by dipping $Ni(OH)_2$/NF into $Co(NO_3)_2$ solution via cation exchange. In solution, $Co^{2+}$ first adsorbs onto the negatively charged $Ni(OH)_2$ surface through electrostatic interactions. An ion exchange reaction then occurs: $Ni(OH)_2 + Co^{2+} \rightarrow NiCo(OH)_x$, which promotes the entry of $Co^{2+}$ into the lattice, replacing $Ni^{2+}$ in $Ni(OH)_2$ to form a $NiCo(OH)_x$ solid solution. At 300 °C in air, $NiCo(OH)_x$ undergoes dehydration and transforms into $NiCo_2O_4$: $NiCo(OH)_2 \rightarrow NiCo_2O_4 + H_2O$. Metal and oxygen ions move and rearrange during this process. At the same time, some $Co^{2+}$ and $Ni^{2+}$ are oxidized into $Co^{3+}$ and $Ni^{3+}$, forming a mixed-valence state, improving the material's electrical conductivity and chemical stability. Of which, the nanosheet shape is maintained to provide fixed active sites for the next sulfuration step. The $NiCoS_x$@$Ni_3S_2$/NF was formed via hydrothermal anion exchange by using thiourea as sulfur source as below. Under hydrothermal conditions at 120 °C, thiourea undergoes a decomposition reaction: $CH_4N_2S + 2H_2O \rightarrow CO_2 + 2NH_3 + H_2S$. At the same time, $NiCo_2O_4$ reacts with sulfide ions ($S^{2-}$) through a substitution reaction: $NiCo_2O_4 + S^{2-} + H^+ \rightarrow NiCoS_x + H_2O$. During this process, Ni, Co, and S elements are co-introduced. The synergistic co-deposition effect suppresses atomic ordering, leading to the formation of an amorphous material with a unique structure. The co-deposition of multiple elements enhances the structural activity of the catalyst and helps improve its catalytic performance.

The elemental composition and crystal structure of the synthesized electrode materials were confirmed by X-ray diffraction (XRD) characterization. As illustrated in Fig. S2, all the samples exhibit the characteristic peaks at 44.5°, 51.9° and 76.5°, which match perfectly with the metal Ni. The XRD patterns of $Ni_3S_2$/NF show the characteristic peaks at 21.7°, 31.1°, 37.8°, 38.3°, 44.3°, 49.7°, 50.1°, and 54.6°, corresponding to the (101), (110), (003), (021), (202), (113), (211), and (104) crystal planes of $Ni_3S_2$ (JCPDS 48–0083), respectively. In addition to the characteristic peaks of $Ni_3S_2$, the XRD patterns of $NiCoS_x$@$Ni_3S_2$/NF exhibit distinct diffraction peaks at 26.8°, 47.4°, 50.4°, 65.1°, and 78.2°, corresponding to the (220), (422), (511), (533), and (731) crystal planes of $NiCo_2S_4$ (JCPDS 20–0782), respectively [46]. Yet, the XRD patterns of $NiCoS_x$ exhibit relatively weak diffraction peaks, suggesting its low crystallinity. After extensive etching by Co and S, only the diffraction peaks from the NF substrate remain observable, confirming the complete amorphization of $NiCoS_x$ on the NF surface. Scanning electron microscopy (SEM) and transmission electron microscope (TEM) were performed to study the microstructure of the samples. As shown in Fig. S3, uniform $Ni(OH)_2$/NF nanosheets are formed by etching growth on the NF substrate. Meanwhile, $NiCo(OH)_2$/NF maintains the nanosheet morphology after further exchange of $Ni^{2+}$ with $Co^{2+}$. Furthermore, the $NiCo_2O_4$@NiO/NF nanosheets are formed through oxidative transformation of $NiCo(OH)_2$/NF precursors in air, facilitated by Ni–Co bonding (Fig. 1a, b). The $NiCo_2O_4$@NiO/NF heterostructure displays well-defined lattice fringes with lattice spacing of 0.47 and 0.21 nm, corresponding to the (111) and (200) planes, respectively (Fig. 1c–e), revealing high crystallinity. Furthermore, the $NiCoS_x$@$Ni_3S_2$/NF nanorods are formed by anion exchange method (Fig. 1f). The TEM results prove the presence of nanorods, along with thin layers at their edges (Fig. 1g, h). The HRTEM images reveal that the heterogeneous interface is directly observed at the phase boundary between the $Ni_3S_2$ and $NiCoS_x$ (Fig. 1i). The observed 0.40 nm lattice fringes correspond to the (102) planes of crystalline $Ni_3S_2$, confirming the highly ordered structure in the nanorod core (Fig. 1j). However, the outer low-crystalline layer shows 0.28 and 0.17 nm fringes, matching $NiCoS_x$ (211) and (100) planes, respectively. The above-mentioned structure


https://doi.org/10.1007/s40820-026-02151-6

displays extensive atomic disorder and defects, confirming low crystallinity. This morphology arises from the outward diffusion of $Co^{2+}$ and the inward diffusion of $S^{2-}$, coupled with the formation of nanoarray by $S^{2-}$ etching. Both inner crystalline $Ni_3S_2$ layer (high conductivity) and outer low-crystalline $NiCoS_x$ layer (rich defect) form a precisely tuned heterostructure. The scanning transmission electron microscopy-energy dispersive X-ray spectroscopy (TEM-EDS) analysis reveals the uniform distribution of Co, Ni, and S elements in $NiCoS_x@Ni_3S_2$ nanorod (Fig. S4). Meanwhile, the molar fractions of Ni, S, and Co in $NiCoS_x@Ni_3S_2$ are 61.82%, 36.77%, and 1.40%, respectively (Fig. S5, Supporting Information). For the $Ni_3S_2$/NF sample, the Ni/S atomic ratio is 60.6/39.4, which closely matches the theoretical stoichiometric ratio of 3/2 by using ICP-OES. For the $NiCoS_x$/NF, the overall Ni/Co/S ratio is 58.2/6.7/35.5. For the $NiCoS_x@Ni_3S_2$/NF sample, the Ni/Co/S ratio is 66.2/2.4/31.4, where the Ni signal primarily originates from the core of the substrate. The enrichment of cobalt at the interface is induced by the Ni–S–Co bridging bond. As a control sample, the $Ni_3S_2$ without Co ion exchange treatment maintains vertically aligned convex nanoarray (Fig. S6). The SEM analysis reveals that excessive sulfur etching generates rough nanoarrays of $NiCoS_x$/NF (Fig. S7), while the TEM analysis indicates the formation of an amorphous structure (Fig. S8). Ultraviolet photoelectron spectroscopy (UPS) was employed to probe the interfacial interactions in low-crystalline $NiCoS_x$@crystalline $Ni_3S_2$ heterogeneous interface. The $\Delta\Phi$ is calculated as $\Delta\Phi = h\nu - E_{cutoff}$, where $h\nu$ represents the incident photon energy (21.22 eV) and the $E_{cutoff}$ is derived from the cutoff energy from the UPS measurements. As shown in Fig. S9, the $E_{cutoff}$ value for $NiCoS_x@Ni_3S_2$/NF, $Ni_3S_2$/NF, and $NiCoS_x$/NF is 17.41, 17.74, and 17.13 eV, respectively. The $\Delta\Phi$ value for $NiCoS_x@Ni_3S_2$

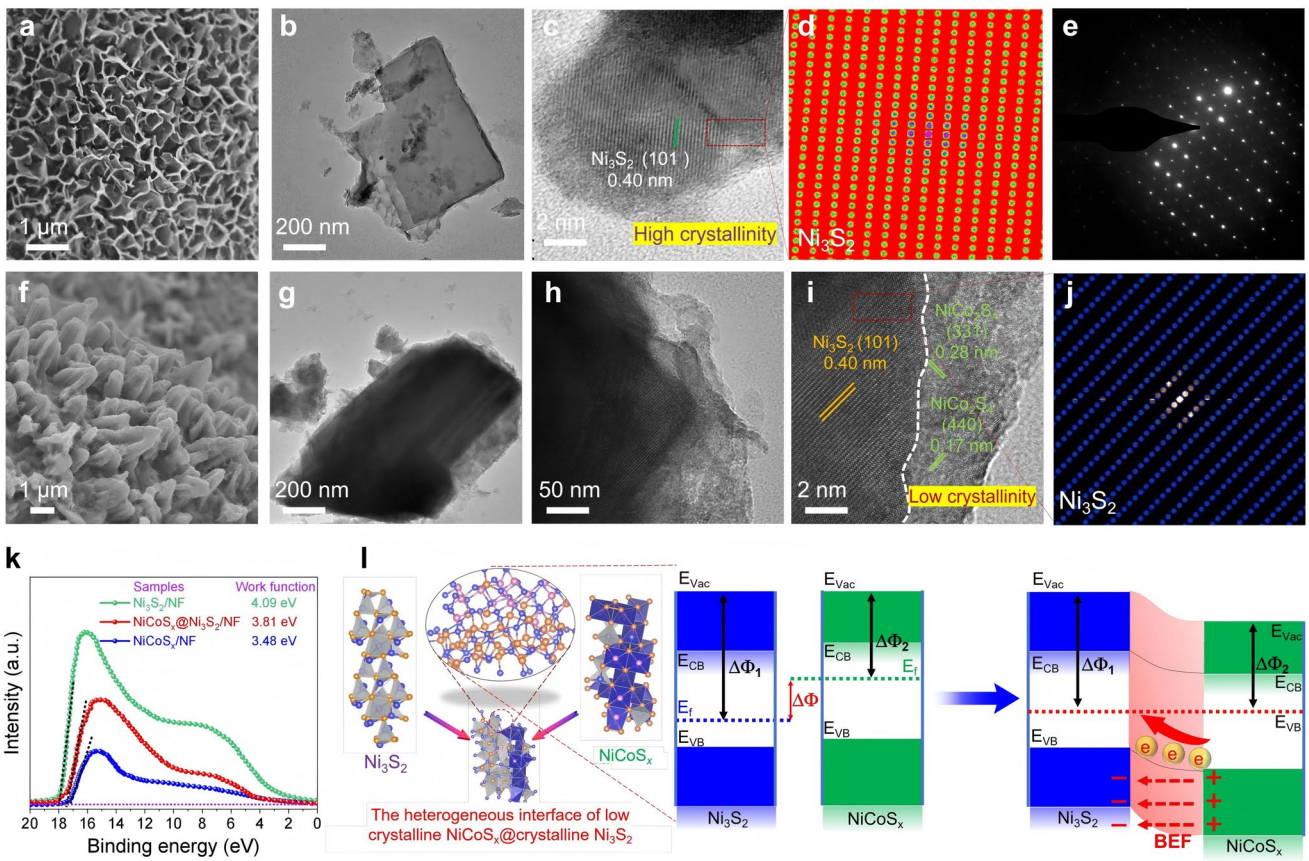


**Fig. 1** Structural characterization. $NiCo_2O_4$@NiO: **a** SEM image, **b** TEM image, **c** HRTEM image, **d** Corresponding high-resolution atomic image and **e** FFT pattern. $NiCoS_x@Ni_3S_2$: **f** SEM image, **g**, **h** TEM images, **i** HRTEM image, **j** Corresponding high-resolution atomic image. **k** UPS spectra of $Ni_3S_2$/NF, $NiCoS_x@Ni_3S_2$/NF, $NiCoS_x$/NF. **l** Schematic diagram of the electron transfer process in the energy band of $NiCoS_x@Ni_3S_2$

($\Delta\Phi = 3.81$ eV) is between that of $Ni_3S_2$/NF ($\Delta\Phi = 4.09$ eV) and $NiCoS_x$/NF ($\Delta\Phi = 3.48$ eV) (Fig. 1k). These values produce an asymmetric concentration gradient of electrons, creating a BEF in the direction of the $\Delta\Phi$ from low value ($NiCoS_x$) to high value ($Ni_3S_2$). Furthermore, the band diagrams demonstrate the BEF-driven electron transfer from $NiCoS_x$ to the $NiCoS_x$@$Ni_3S_2$ interface, and ultimately to $Ni_3S_2$, realizing new equilibrium state (Fig. 1l). The BEF helps to reduce the energy barrier for electron escape from the surface of material, thereby promoting electron transfer. Therefore, synergistic chemical bond coupling and BEF-driven charge redistribution at the heterointerface enhance electron transfer and optimize intrinsic activity.

The surface chemical compositions and valence distributions of Ni, Co and S in $Ni_3S_2$/NF, $NiCoS_x$/NF and $NiCoS_x$@$Ni_3S_2$/NF were analyzed by XPS technique. As shown in Fig. 2a, the binding energies of 855.5/861.0 and 873.1/879.2 eV correspond to the characteristic peaks of $Ni^{2+}$ and $Ni^{3+}$, which are assigned to Ni $2p_{3/2}$ and Ni $2p_{1/2}$, respectively. The binding energies of 780.3 and 783.2 eV correspond to the characteristic peaks of $Co^{2+}$ and $Co^{3+}$ (Fig. 2b). The main peak in the S 2*p* XPS spectra at 161.6 and 163.4 eV is assigned to the S–O bond and metal-S bond, respectively (Fig. 2c). Notably, XPS analysis reveals that a positive shift of 0.7 eV in the binding energy of Ni 2*p* indicates the oxidation $Ni^{3+}$ from $Ni^{2+}$, and a positive shift of 0.4 eV in the Co 2*p* binding energy confirms the formation of $Co^{3+}$. Concurrently, the S 2*p* binding energy exhibits negative shifts of 0.4 and 0.8 eV, respectively, collectively attributing to interfacial electron transfer from Ni and Co to S. In the heterostructure, Ni $2p_{3/2}$ and Co $2p_{3/2}$ peaks shift positively relative to the pure phases, indicating partial electron depletion on the shell side, while the negative shift of the S 2*p* peaks suggests stronger metal-S interactions. The optimized charge redistribution at the heterointerface enhances the adsorption energy of OER intermediates (*OH → *O) and improves $H_2O$ dissociation kinetics. This synergistic effect originates from the heterointerface between the low-crystalline $NiCoS_x$ layer and the crystalline $Ni_3S_2$ phase, which facilitates rapid electron transfer and stabilizes the active sites, ultimately achieving high catalytic activity.

X-ray absorption spectroscopy techniques, including XANES and extended X-ray absorption fine structure (EXAFS) spectra were explored to probe the electronic properties, valence states, and local coordination environments of $Ni_3S_2$, $NiCoS_x$, and $NiCoS_x$@$Ni_3S_2$. Ni K-edge XANES shows the pre-edge positive peak shifts of $NiCoS_x$@$Ni_3S_2$ versus $Ni_3S_2$, indicating that Co promotes Ni to higher oxidation states (Fig. 2d). Co K-edge XANES reveals a slight pre-edge peak downshift of $NiCoS_x$@$Ni_3S_2$ versus $NiCoS_x$ (Fig. 2g). The results indicate an electron transfer pathway from $NiCoS_x$ to $NiCoS_x$@$Ni_3S_2$, subsequently to $Ni_3S_2$, in agreement with the XPS and UPS results. R-space resolution analysis reveals two prominent coordination peaks at the Ni and Co K-edges of $NiCoS_x$@$Ni_3S_2$ at 1.76 and 1.82 Å, corresponding to Ni-S and Co-S bonds, respectively. Moreover, $NiCoS_x$@$Ni_3S_2$ exhibits shorter Ni–S (1.87 Å) and Co–S (1.89 Å) bonds than pure phases, indicating stronger interfacial bonding (Fig. 2e, h). The EXAFS spectra are fitted to investigate the coordination environment and coordination number (CN) of $NiCoS_x$@$Ni_3S_2$ (Fig. 2f, i and Table S1). The EXAFS analysis of $NiCoS_x$@$Ni_3S_2$ confirms the Ni–S bond (2.05 Å, CN = 2.7) and Co-S (2.11 Å, CN = 2.11) bond. The shortening of the Ni–S and Co–S bond length is ascribed to the formation of Ni–S–Co interfacial bridge in $NiCoS_x$@$Ni_3S_2$. Wavelet transform analysis of Ni K-edge EXAFS oscillations is probed to investigate the atomic dispersion properties (Fig. 2j). The maximum intensity of the Ni foil at 2.3 Å, and Co foil at 2.1 Å is ascribed to the electronic contributions of both Ni–Ni and Co–Co bond, respectively. The maximum intensity of $NiCoS_x$@$Ni_3S_2$ at 1.5 and 1.8 Å is plausibly interpreted as the contribution of the Ni–S bond and Co–S bond. These values are smaller than the maximum intensity of the pure Ni and Co foil. Overall, these findings demonstrate that the low-crystalline $NiCoS_x$ shell and crystalline $Ni_3S_2$ core undergo significant interfacial charge redistribution, effectively stabilizing lattice sulfur. The resulting Ni–S–Co interfacial bridges create new electron-transfer pathways, which not only suppress oxidative degradation during OER but also enhance both the activity and durability of $NiCoS_x$@$Ni_3S_2$ compared to single-phase catalysts.

Compared with conventional sulfide catalysts (e.g., $NiCo_2S_4$, $Co_9S_8$, $Ni_3S_2$), the low-crystalline $NiCoS_x$ shell is the critical component for enhancing the overall water splitting performance of $NiCoS_x$@$Ni_3S_2$, with core contributions [47–51]: 1) Atomic disorder and abundant defects boost the exposure of unsaturated coordination active sites, as reflected by high electrochemical active surface area (ECSA) of the catalyst; 2) The work function difference between low-crystalline $NiCoS_x$ and crystalline $Ni_3S_2$ induces a built-in

 https://doi.org/10.1007/s40820-026-02151-6

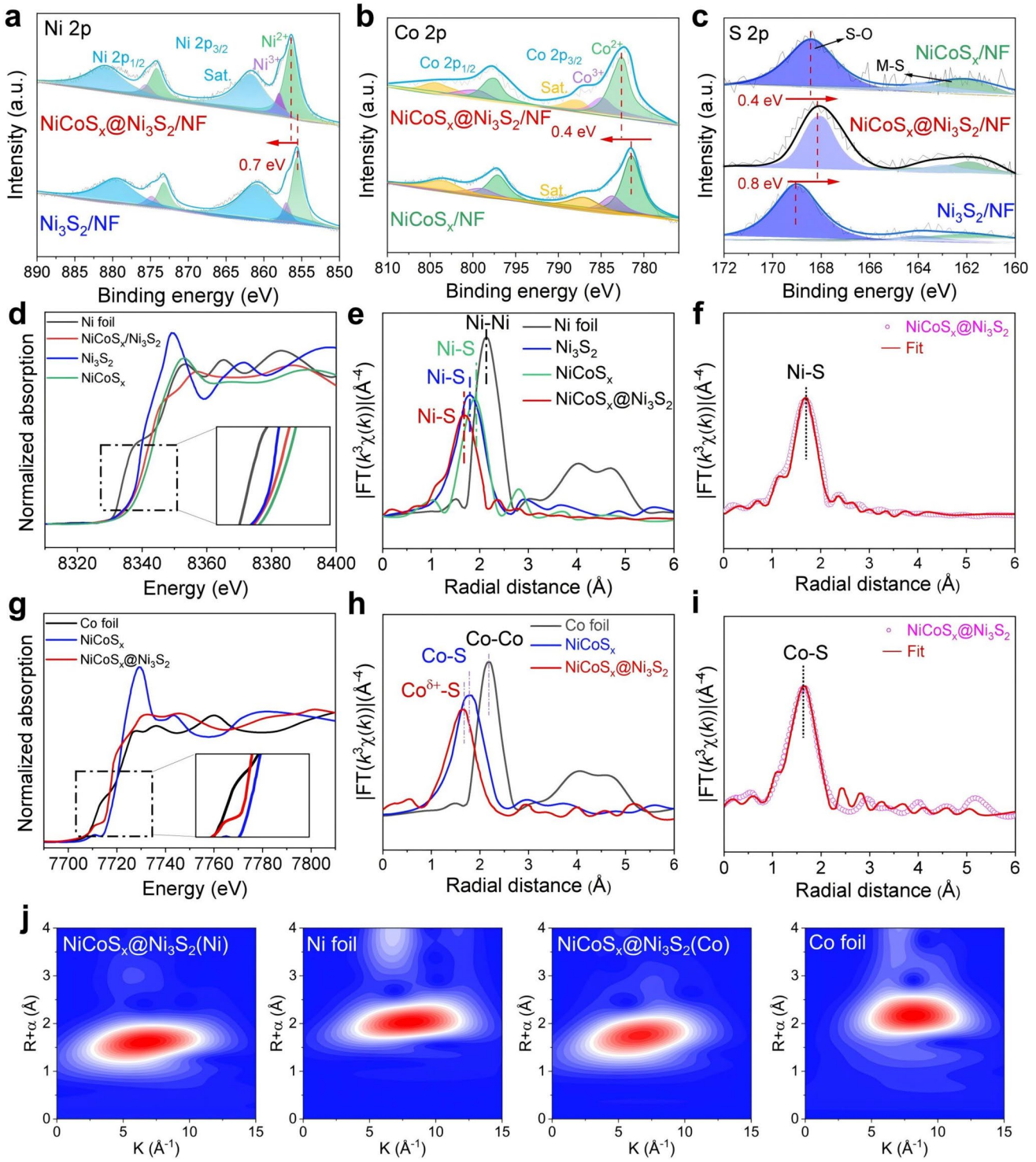


**Fig. 2** Electronic configuration and atomic structure. XPS spectra of $Ni_3S_2$, $NiCoS_x$, and $NiCoS_x@Ni_3S_2$: **a** Ni 2*p*, **b** Co 2*p*, **c** S 2*p*. **d**, **g** XANES spectra. **e**, **h** $k^3$-weighted EXAFS spectra. **f**, **i** FT-EXAFS fitting results. **j** wavelet transform WT of $Ni_3S_2$, $NiCoS_x@Ni_3S_2$, Ni foil and Co foil

electric field, which, coupled with Ni–S–Co interfacial bridges, optimizes the d-band center of Ni/Co active sites and facilitates directional charge transfer, laying the groundwork for accelerated reaction kinetics. These structural and electronic merits of the low-crystalline $NiCoS_x$ shell, in synergy with the high-conductivity crystalline $Ni_3S_2$ core, are expected to responsible for the superior HER and OER performance of $NiCoS_x$@$Ni_3S_2$ as elaborated in the following sections.

### 3.2 Hydrogen Evolution Catalysis

The HER performance of $NiCoS_x$@$Ni_3S_2$/NF was systematically evaluated against control samples ($NiCoS_x$/NF, $Ni_3S_2$/NF, $NiCo_2O_4$@NiO/NF) via a three-electrode system. As shown in Fig. 3a, b, $NiCoS_x$@$Ni_3S_2$/NF consistently exhibits the lowest overpotentials across all tested conditions, requiring 44, 123, and 346 mV at 10, 100, and 1000 mA $cm^{-2}$, respectively. This demonstrates its excellent catalytic activity and remarkable stability under high current densities. In contrast, Pt/C/NF shows strong performance at low current densities (32 mV at 10 mA $cm^{-2}$), but its overpotential increases sharply to 384 mV at 1000 mA $cm^{-2}$, indicating poor stability at high currents. Notably, the $\eta_{10}$ value of $NiCoS_x$@$Ni_3S_2$/NF outperforms that of most other related transition metal sulfide-based composites (Fig. 3c, Table S2). In contrast, commercial Pt/C possesses the best HER activity, but Pt/C is disadvantageous at high current densities (> 712 mA $cm^{-2}$). Tafel plots analysis from LSV data reveals the HER kinetics and intrinsic catalytic activity. The $NiCoS_x$@$Ni_3S_2$/NF shows superior HER kinetics (Tafel slope = 46.8 mV $dec^{-1}$) versus controls samples: NF (198.5 mV $dec^{-1}$), $NiCoS_x$/NF (158.9 mV $dec^{-1}$), $Ni_3S_2$/NF (110.5 mV $dec^{-1}$), and $NiCo_2O_4$@NiO/NF (59.7 mV $dec^{-1}$) (Fig. 3d).

To reflect HER kinetics more accurately, the Tafel slope is calculated by steady-state polarization at constant potentials. Specifically, chronoamperometry (CA) was performed for 150 s of steady-state current density in the voltage of − 0.45 ~ 0 V versus RHE. The Tafel slope of $NiCoS_x$@$Ni_3S_2$/NF for the steady-state polarization method is 57.9 mV $dec^{-1}$, which is significantly better than the comparison samples of NF (210.5 mV $dec^{-1}$), $NiCoS_x$/NF (169.3 mV $dec^{-1}$), $Ni_3S_2$/NF (122.5 mV $dec^{-1}$), and $NiCo_2O_4$@NiO/NF (70.3 mV $dec^{-1}$) (Fig. 3e). The steady-state and instantaneous Tafel slopes show similar trends, confirming that $NiCoS_x$@$Ni_3S_2$/NF accelerates the rate-determining steps of Volmer-Heyrovsky in HER (Figs. S10–S13). In addition, the $NiCoS_x$@$Ni_3S_2$/NF electrode exhibits excellent durability, maintaining a stable current density of 1000 mA $cm^{-2}$ for 48 h with negligible decay. Moreover, the polarization curves before and after 3000 cycles nearly overlap, confirming its robust catalytic activity and structural stability for practical HER applications (Fig. 3f). The TOF value of $NiCoS_x$@$Ni_3S_2$ (265 $s^{-1}$) is significantly bigger than that of $NiCo_2O_4$@NiO/NF (132 $s^{-1}$), $Ni_3S_2$/NF (41 $s^{-1}$) and $NiCoS_x$/NF (19 $s^{-1}$) at 50 mV, reflecting superior intrinsic HER activity (Figs. S14 , S15). $NiCoS_x$@$Ni_3S_2$/NF shows the highest ECSA (25.1 mF $cm^{-2}$) compared with $NiCo_2O_4$@NiO/NF (12.9 mF $cm^{-2}$), $Ni_3S_2$/NF (10.1 mF $cm^{-2}$) and $NiCoS_x$/NF (5.2 mF $cm^{-2}$) (Figs. S16, S17), demonstrating the sulfur defects and low crystallinity boost the exposure of the active site. Furthermore, electrochemical impedance spectroscopy (EIS) measurements were conducted to probe charge transfer kinetics. The $NiCoS_x$@$Ni_3S_2$/NF demonstrates the lowest charge transfer resistance ($R_{ct}$ = 7.2 Ω), smaller than other control samples: NF (> 16 Ω), $Ni_3S_2$/NF (9.1 Ω), $NiCoS_x$/NF (11.6 Ω) (Fig. 3g). Operando EIS is used to probe the charge transfer mechanism of HER in $Ni_3S_2$/NF, $NiCo_2O_4$@NiO/NF and $NiCoS_x$@$Ni_3S_2$/NF across 0 to − 80 mV, with Bode plot analysis (Fig. 3h). The high-frequency region of Bode phase plots reflects the electron transfer between catalyst bulk and active sites, corresponding to the Volmer step. Conversely, the mid- and low-frequency regions are indicative of the Heyrovsky step. The HER proceeds via the Volmer-Heyrovsky pathway, where chemisorbed H atoms react with $H_2O$ to generate $H_2$. The frequency peak gradually decreases and shifts to higher frequencies as the applied potential decreases. This indicates the reduced charge-transfer resistance at the catalyst-electrolyte interface with enhanced reaction kinetics. Notably, $NiCoS_x$@$Ni_3S_2$/NF exhibits both reduced phase angles and accelerated high-frequency peak shifts compared to $Ni_3S_2$/NF and $NiCo_2O_4$@NiO/NF at the equal potentials. Thus, the $NiCoS_x$@$Ni_3S_2$/NF promotes the adsorption of water and hydrogen, resulting in accelerated HER kinetics.

### 3.3 Oxygen Evolution Catalysis

Given its exceptional HER performance, $NiCoS_x$@$Ni_3S_2$/NF demonstrates equally outstanding OER activity. As

 https://doi.org/10.1007/s40820-026-02151-6

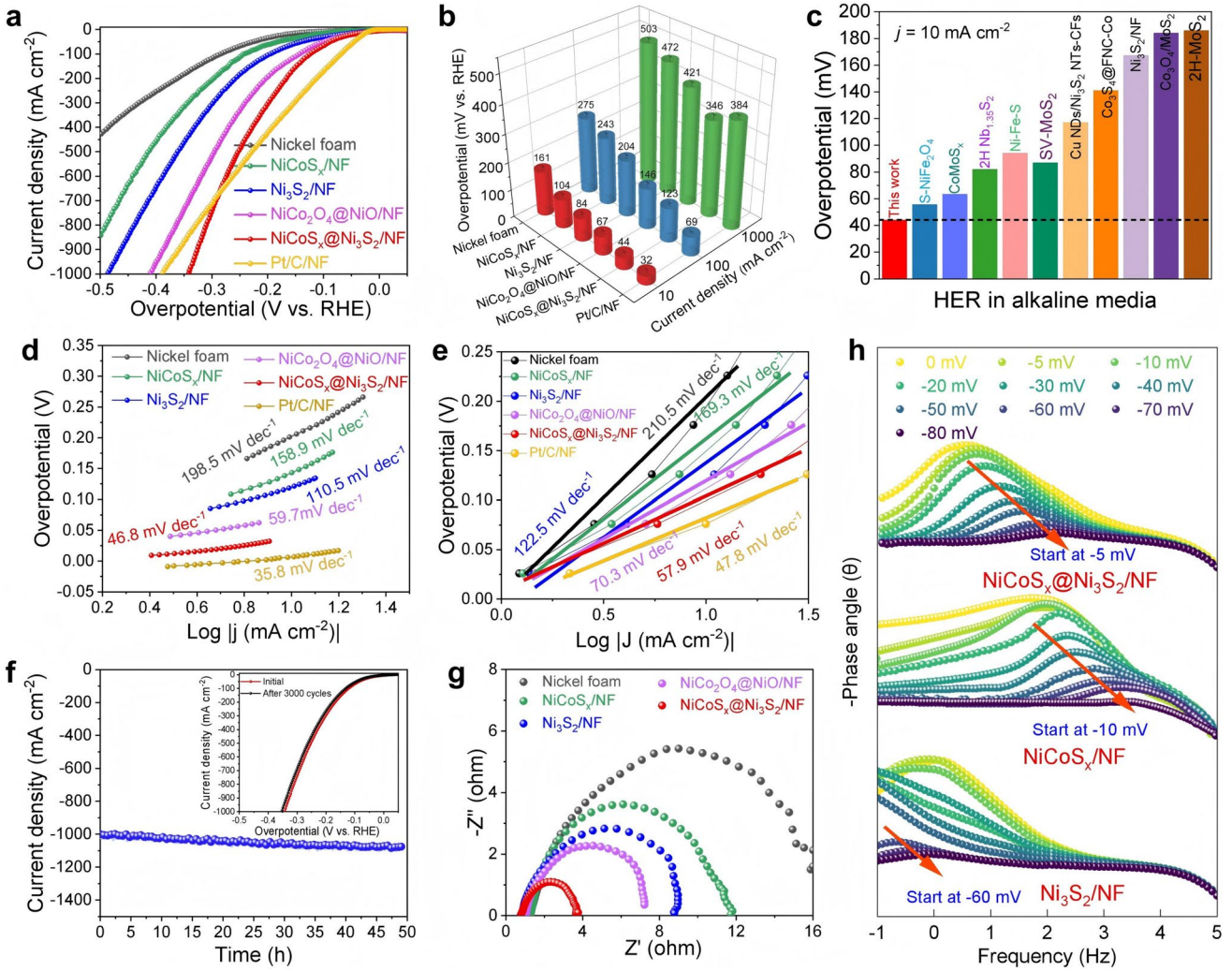


**Fig. 3** HER catalytic activity of $Ni_3S_2$/NF, $NiCoS_x$/NF, $NiCo_2O_4$@NiO/NF, $NiCoS_x$@$Ni_3S_2$/NF and Pt/C/NF in 1.0 M KOH solution: **a** LSV polarization curves, **b** Comparison of overpotentials at 10, 100, and 1000 mA $cm^{-2}$. **c** Comparison of HER performance among the reported electrocatalysts. **d** Tafel plots. **e** Steady-state polarization Tafel curves. **f** Current density time-dependent test of $NiCoS_x$@$Ni_3S_2$/NF. **g** Nyquist plots. **h** Phase angle plots of EIS data at various voltages for $Ni_3S_2$/NF, $NiCoS_x$/NF and $NiCoS_x$@$Ni_3S_2$/NF

shown in Fig. 4a, the OER polarization curves reveal that $NiCoS_x$@$Ni_3S_2$/NF delivers the highest current densities at lower overpotentials compared with other electrodes, including bare NF, $Ni_3S_2$/NF, $NiCoS_x$@$Ni_3S_2$/NF, $NiCo_2O_4$@NiO/NF and $RuO_2$/NF. This superior performance is further quantified in Fig. 4b, where $NiCoS_x$@$Ni_3S_2$/NF exhibits the lowest overpotentials of 212, 342, and 520 mV at 10, 100, and 1000 mA $cm^{-2}$, respectively. In comparison, $RuO_2$/NF, $Ni_3S_2$/NF and $NiCo_2O_4$@NiO/NF exhibit significantly higher overpotentials. The remarkable OER activity of $NiCoS_x$@$Ni_3S_2$/NF is attributed to the synergistic effect of the heterostructured interface, which facilitates rapid charge transfer and optimizes the exposure of active sites, thereby enabling both low onset potential and robust catalytic efficiency under high current densities. Notably, the $\eta_{10}$ value of $NiCoS_x$@$Ni_3S_2$/NF surpasses that of reported TMS-based composites (Fig. 4c, Table S3). The $NiCoS_x$@$Ni_3S_2$/NF demonstrates superior OER performance, exhibiting a significantly lower Tafel slope (58.9 mV $dec^{-1}$) compared to control samples (NF: 295.6 mV $dec^{-1}$, $NiCoS_x$/NF: 141.9 mV $dec^{-1}$, $Ni_3S_2$/NF: 117.2 mV $dec^{-1}$, and $NiCoS_x$@$Ni_3S_2$/NF: 98.5 mV $dec^{-1}$) (Fig. 4d).

For consistent OER kinetic analysis, Tafel slopes are derived from steady-state polarization at constant potentials, following the same methodology employed for HER analysis (Figs. 4e, S18 and S19). The transient Tafel slopes

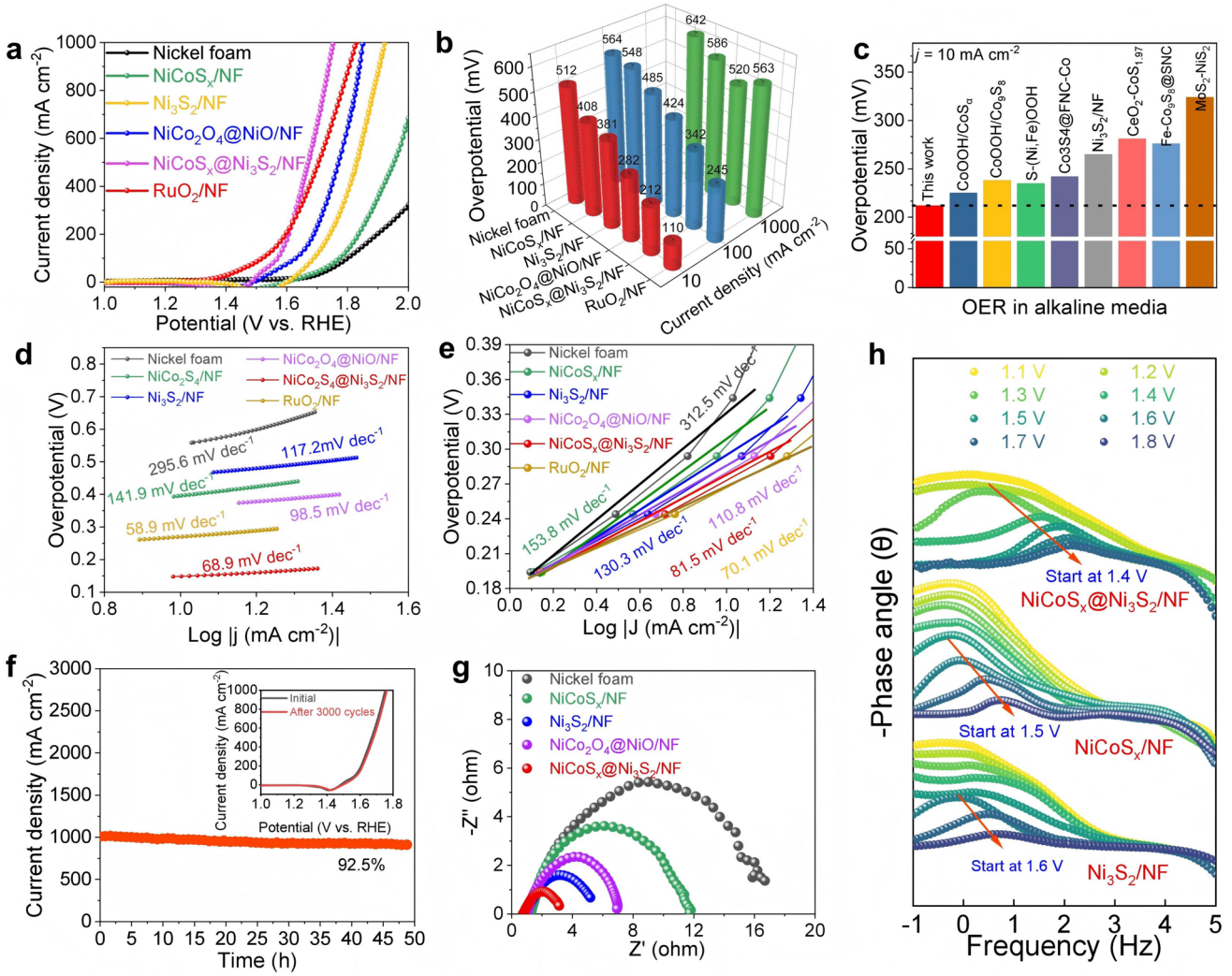


**Fig. 4** OER catalytic activity of $Ni_3S_2$/NF, $NiCoS_x$/NF, $NiCo_2O_4$@NiO/NF, $NiCoS_x$@$Ni_3S_2$/NF and $RuO_2$/NF in 1.0 M KOH solution: **a** LSV polarization curves, **b** Comparison of overpotentials at 10, 100, 1000 mA $cm^{-2}$. **c** Comparison of OER performance among the reported electrocatalysts. **d** Tafel plots. **e** Steady-state polarization Tafel curves. **f** Current density time-dependent test of $NiCoS_x$@$Ni_3S_2$/NF. **g** Nyquist plots. **h** Phase angle plots of EIS data at various voltages for $Ni_3S_2$/NF, $NiCoS_x$/NF and $NiCoS_x$@$Ni_3S_2$/NF

of these materials are consistent with the Tafel slopes of the steady state polarization method (Fig. S20). In electrocatalytic reaction kinetics, the difference between steady-state and transient Tafel slopes primarily arises from the dynamic adsorption equilibrium of intermediates on the electrode surface (Figs. S13 and S20). The steady-state Tafel slope of $NiCoS_x$@$Ni_3S_2$/NF is higher than the transient one, which is explained by the following factors: (1) During steady-state polarization, the continuous application of potential leads to the gradual accumulation of H*/*OH intermediates on the active sites, creating an additional adsorption energy barrier; (2) The low crystallinity and high defect density of the $NiCoS_x$ layer provide more intermediate adsorption sites, further hindering charge transfer; (3) The heterojunction interface undergoes dynamic reconstruction under prolonged polarization, and some active sites become passivated. In contrast, transient measurements capture the intrinsic kinetics of the initial electron transfer step, where intermediate accumulation is not yet significant, thus reflecting the theoretical kinetics more accurately. The TOF value of $NiCoS_x$@$Ni_3S_2$/NF (126 $s^{-1}$) at the overpotential of 400 mV is significantly higher than that of $NiCoS_x$/NF (17 mV $dec^{-1}$), $Ni_3S_2$/NF (39 mV $dec^{-1}$) and $NiCo_2O_4$@NiO/NF (75 mV $dec^{-1}$), which is consistent with the performance of OER


https://doi.org/10.1007/s40820-026-02151-6

(Figs. S21, S22). In addition, the $NiCoS_x$@$Ni_3S_2$/NF electrode maintains 92.5% of its initial current density after 48 h at 1000 mA $cm^{-2}$, and the polarization curves before and after 3000 cycles nearly overlap, confirming its excellent durability and structural stability for OER (Fig. 4f). As illustrated in Figs. S23 and S24, the $NiCoS_x$@$Ni_3S_2$/NF exhibits the highest ECSA of 21.4 mF $cm^{-2}$, surpassing that of $NiCo_2O_4$@NiO/NF (16.0 mF $cm^{-2}$), $Ni_3S_2$/NF (9.8 mF $cm^{-2}$), and $NiCoS_x$/NF (2.0 mF $cm^{-2}$). In addition, the increased ECSA value indicates that the low-crystalline structure effectively increases the accessibility of superior active sites. The $NiCoS_x$@$Ni_3S_2$/NF demonstrates the lowest charge transfer resistance ($R_{ct}$ = 3.1 Ω), surpassing contrast samples: $NiCo_2O_4$@NiO/NF (7.1 Ω), $Ni_3S_2$/NF (5.2 Ω), $NiCoS_x$/NF (12 Ω), and NF (17 Ω) (Fig. 4g). Moreover, operando EIS measurements on $Ni_3S_2$/NF, $NiCoS_x$/NF and $NiCoS_x$@$Ni_3S_2$/NF provide deeper insight into the kinetics of the water oxidation reaction (Fig. 4h). Notably, the high-frequency region ($10^2$–$10^4$ Hz) reflects inner-layer electron transfer from bulk to surface active sites, while the low-frequency range ($10^{-2}$ ~ $10^2$ Hz) reveals interfacial charge transfer at the catalyst/electrolyte interface. The $NiCoS_x$@$Ni_3S_2$/NF shows OER phase angle reduction at 1.4 V through low-frequency phase angle, outperforming $NiCo_2O_4$@NiO/NF (1.5 V) and $Ni_3S_2$/NF (1.6 V). The $NiCoS_x$@$Ni_3S_2$/NF exhibits reduced peak intensities across both the frequency domains, with accelerated attenuation as the applied potential increases. These results suggest that the low-crystalline $NiCoS_x$-tuned crystalline $Ni_3S_2$ heterogeneous interface enhances both capacitive behavior and -OH adsorption, accelerating OER kinetics.

### 3.4 Cation and Anion Exchange Regulation Mechanism

In both cation exchange and anion exchange sulfidation processes, etching temperature and reaction time collaboratively regulate the catalyst's morphology, composition, phase structure, and defect characteristics, establishing a precise "structure-performance" relationship that determines its bifunctional HER/OER electrocatalytic activity.

Temperature regulates the thermodynamic and kinetic balance of ion exchange, thereby precisely controlling $Co^{2+}$ doping efficiency, morphology, and crystallinity (Fig. S25). At 40 °C, ion exchange is slow, leading to incomplete $Co^{2+}$ doping, disordered morphology, and limited active site exposure. At 80 °C, the morphology becomes more regular, and site exposure improves. At 120 °C, the system reaches thermodynamic equilibrium, with arrays becoming more regular and dispersed, and the active site exposure reaches its peak. ICP-MS results show that the Co/Ni ratio increases from 0.012 at 40 °C to 0.036 at 120 °C due to accelerated Ni dissolution and Co enrichment, which matches the moderately low crystallinity structure (Fig. S26). As the $Co^{2+}$ exchange temperature increases, the EPR signal intensity gradually strengthens, indicating that higher temperatures promote the incorporation of $Co^{2+}$ into the carrier lattice, thereby inducing a higher concentration of lattice defects (Fig. S27). The LSV curves for HER and OER at different $Co^{2+}$ exchange temperatures indicate that the optimal catalytic activity occurs at 120 °C, while 160 °C results in decreased performance (Fig. S28).

Time governs the morphological evolution and $Co^{2+}$ doping depth, impacting active site exposure and mass transfer efficiency (Fig. S29). At 0.5 h, the catalyst is a dense substrate with limited active sites and low mass transfer efficiency. After 1 h, discrete nanosheets form, but the structure lacks regularity. After 3 h, the nanosheets crosslink into an open layered structure, achieving the optimal synergy between active site exposure and mass transfer efficiency. At 6 h, excessive growth and agglomeration bury the active sites, leading to performance degradation. ICP-MS and electrochemical tests confirm that at 3 h, the Co/Ni ratio is 0.036, with the optimal synergy between doping and morphology, resulting in the best HER/OER activity (Figs. S30 and S31).

Sulfidation time regulates the morphology, phase structure, and defect concentration of the catalyst. From 0.5 to 2 h, the surface forms nanostructures like nanospikes, particles, and discrete nanosheets, with poor site exposure and mass transfer (Fig. S32). After 3 h, a flower-like array (the optimal morphology) forms, significantly improving site exposure and mass transfer efficiency. At 6 h, excessive growth and agglomeration bury the active sites. The XRD result shows that after 3 h, a highly crystalline $NiCoS_x$@$Ni_3S_2$ heterojunction is formed, while after 6 h, it transitions to a pure-phase $NiCoS_x$, losing the heterojunction advantage (Fig. S33). Electron paramagnetic resonance (EPR) spectroscopy was employed to detect defect-induced unpaired electrons, confirming the low-crystalline nature of $NiCoS_x$@$Ni_3S_2$. Intensive sulfide etching amplifies these defects, with the defect concentration initially increasing and peaking at 3 h, providing the most active sites. After 6 h, excessive

defects reduce stability (Fig. S34). Electrochemical tests confirm that 3 h is the optimal sulfidation time (Fig. S35).

Temperature significantly affects the morphology, phase, and defects of the catalyst during sulfidation (Fig. S36). At 80 °C, the catalyst forms a loose fibrous structure, with poor mass transfer and stability. At 120 °C, the catalyst forms dense aggregates with low porosity and insufficient active sites. At 160 °C, the catalyst forms a high surface area flower-like array (the optimal morphology) (Fig. S37). At 200 °C, severe agglomeration leads to the loss of structural advantages. The XRD result shows that at 160 °C, high crystallinity target sulfide phases are formed, enhancing electron transport. At 200 °C, the target phase proportion decreases. The EPR results show that at 160 °C, defect concentration and active site exposure are optimally balanced. Electrochemical tests confirm that the HER/OER activity is the best at 160 °C (Fig. S38).

Thus, cation exchange (120 °C, 3 h) and anion exchange sulfidation (3 h, 160 °C) collaboratively regulate the morphology, phase and defects of the catalyst. This precise optimization achieves the optimal balance between active site exposure, structural stability, and electron transport efficiency, maximizing its bifunctional electrocatalytic performance.

### 3.5 Surface Reconstruction Dynamics and Corrosion Resistance in OER

Oxygen evolution catalysis operando raman spectroscopy was employed to dynamically monitor the surface reconstruction and oxidative corrosion of sulfur species, providing insights into the evolution of electrocatalytic active centers. As shown in Fig. 5a, b, Raman spectroscopy analysis identifies characteristic peaks at 271 ~ 285 $cm^{-1}$ (attributed to the Ni-S phase) and at 462 ~ 477/547 ~ 558 $cm^{-1}$ (attributed to Ni–O phase in Ni–OOH). The Ni–S phase peak of $NiCoS_x$@$Ni_3S_2$/NF and $Ni_3S_2$/NF completely disappears at 1.52 and 1.15 V, respectively. This confirms that low-crystalline $NiCoS_x$ stabilizes metal-sulfur (M-S) bond in crystalline $Ni_3S_2$, effectively enhancing catalytic stability via suppressing sulfide oxidation and corrosion to some degree. Simultaneously, the $NiCoS_x$@$Ni_3S_2$ heterointerface promotes spontaneous Ni–OOH formation at lower open circuit potential (OCP) than $Ni_3S_2$/NF (1.20 V) through interfacial electron redistribution, reducing the activation potential. The oxidation mechanism achieves breakthrough performance through synergistic effects as below: (1) The heterogeneous interface of $NiCoS_x$/$Ni_3S_2$ promotes low-potential Ni–OOH generation, boosting catalytic kinetics via synergistic surface amorphization and active-phase reconstruction. (2) Co-induced amorphous $NiCoS_x$ surface enables dynamic phase reconstruction, achieving high yet balanced activity and stability for OWS via an interface engineering strategy. What's more, the surface intermediate evolution dynamics of $NiCoS_x$@$Ni_3S_2$/NF and $Ni_3S_2$/NF across a 1.0 ~ 1.7 V potential window were probed via in-situ FTIR spectroscopy. In-situ FTIR spectra revealed that both catalysts exhibited distinct characteristic signals attributable to $OOH_{ads}$, M–O* and $OH_{ads}$ species, with signal intensities escalating monotonically with increasing applied potential. Notably, $Ni_3S_2$ displays substantially intensified M–O* and $OH_{ads}$ signals, a hallmark of adsorbate evolution mechanism (AEM) relying on surface intermediate accumulation (Fig. 5c). By contrast, weaker intermediate signals of $NiCoS_x$@$Ni_3S_2$/NF imply predominant lattice oxygen evolution mechanism (LOM) contribution (Fig. 5d). Collectively, these findings confirm that the amorphous $NiCoS_x$ outer layer on $NiCoS_x$@$Ni_3S_2$/NF induces sulfur-oxygen substitution to form an oxygen-rich surface, which elevates LOM contribution, promotes reconstruction into M-OOH, and boosts OER performance (Fig. 5e). In situ XPS technique at various applied potentials was employed to monitor potential-dependent evolution of electronic structures during OER. As shown in the Fig. 5f, g, the concentration of $Ni^{3+}$ species on $Ni_3S_2$ progressively accumulates as the applied potential increases, accompanied by a positive shift in the Ni 2*p* binding energy. This result suggests electron transfer along the Ni-S coordination direction, leading to the oxidation of Ni species. Compared to $Ni_3S_2$, the $NiCoS_x$@$Ni_3S_2$/NF shows stable $Ni^{3+}$ valence state in Ni 2*p* XPS spectra, confirming the stability of valence during electrocatalysis (Fig. 5h).

During OER polarization, $NiCoS_x$@$Ni_3S_2$/NF maintains persistent Co-S/Ni-S bonds, but $Ni_3S_2$/NF shows progressive bond degradation, demonstrating the enhanced structural stability of the former. As the OER potential increases, the Co–S/Ni–S bonding signals in $Ni_3S_2$/NF exhibit significant attenuation, while those remain stable in $NiCoS_x$@$Ni_3S_2$/NF. Therefore, the incorporation of Co and S into $NiCoS_x$@$Ni_3S_2$/NF endows the catalyst with dual functionality: it facilitates surface reconstruction and stabilizes the M–S bonds, thereby achieving an optimal balance between

 https://doi.org/10.1007/s40820-026-02151-6

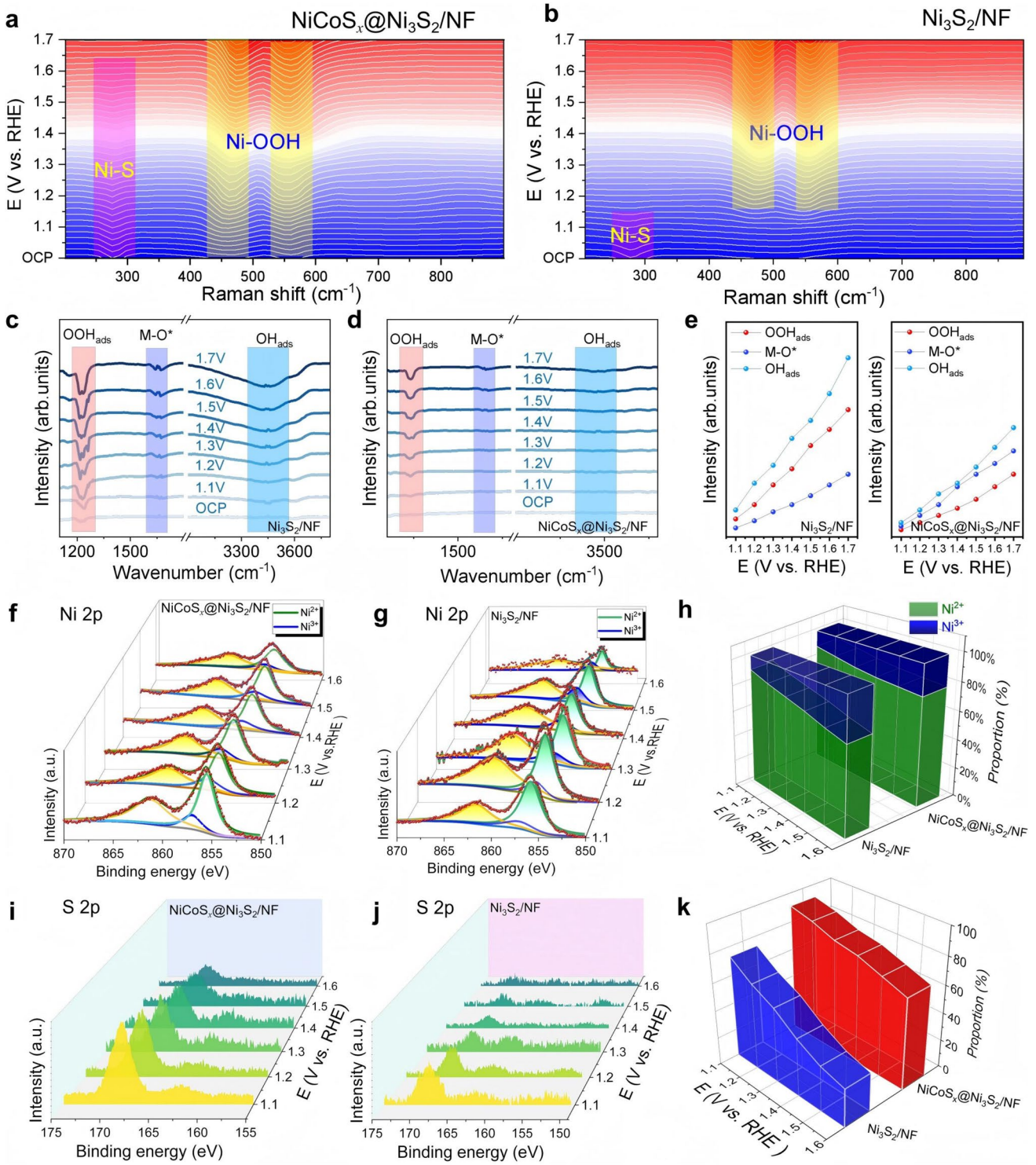


**Fig. 5** Potential-dependent in situ Raman spectra of: **a** $NiCoS_x@Ni_3S_2/NF$, **b** $Ni_3S_2/NF$. In situ FTIR spectra of **c** $Ni_3S_2/NF$ and **d** $NiCoS_x@Ni_3S_2/NF$ catalyst under different applied potentials. **e** Variation in Raman signal intensity of $OOH_{ads}$, M–O, and $OH_{ads}$ species on $NiCoS_x@Ni_3S_2/NF$ and $Ni_3S_2/NF$ catalysts with applied potential. XPS spectra of Ni 2*p*: **f** $NiCoS_x@Ni_3S_2/NF$, **g** $Ni_3S_2/NF$ under different potentials. **h** XPS fitting analysis results of $Ni^{2+}$ and $Ni^{3+}$ ratios for $Ni_3S_2/NF$ and $NiCoS_x@Ni_3S_2/NF$ under different potentials. XPS spectra of S 2*p*: **i** $NiCoS_x@Ni_3S_2/NF$, **j** $Ni_3S_2/NF$ under different potentials. **k** Characteristic peaks of sulfur as percentage of S 2*p* for $Ni_3S_2/NF$ and $NiCoS_x@Ni_3S_2/NF$ under different potentials

catalytic activity and structural durability. In situ S 2*s* XPS spectra show that, at potentials ranging from 1.1 to 1.6 V (vs. RHE), the shifts in binding energy and intensity of sulfur species for $NiCoS_x$@$Ni_3S_2$/NF are significantly more pronounced than those for $Ni_3S_2$/NF (Fig. 5i, j). Quantitative results further demonstrate that $NiCoS_x$@$Ni_3S_2$/NF maintains a higher proportion of active sulfur species across all applied potentials (Fig. 5k), confirming that $NiCoS_x$ modification enriches active sulfur sites and thereby enhance electrocatalytic performance and stability.

These findings confirm that, while complete suppression of sulfide leaching is unattainable under strongly oxidative OER conditions, the $NiCoS_x$ shell substantially mitigates sulfur depletion across a broad operational range. This enhancement is ascribed to the synergistic effects of robust Ni–S–Co interfacial bonding that strengthens lattice sulfur retention, the formation of a reconstructed NiCoOOH-rich surface layer serving as a physical and chemical barrier and a ΔΦ-induced BEF that optimizes interfacial charge distribution and attenuates oxidative degradation at sulfide sites.

### 3.6 Evaluation of Overall Water Splitting and Device Applications

The comprehensive OWS performance was evaluated by constructing radar charts from HER and OER metrics ($\eta_{10}$, TOF, Tafel slope, $R_{ct}$, $C_{dl}$). As shown in the Fig. 6a, b, $NiCoS_x$@$Ni_3S_2$/NF exhibits the largest enclosed area, demonstrating superior HER and OER performance compared to the $NiCo_2O_4$@NiO/NF and $Ni_3S_2$/NF counterparts. Based on the bifunctional catalytic advantages of $NiCoS_x$@$Ni_3S_2$/NF, a symmetric electrolyzer ($NiCoS_x$@$Ni_3S_2$/NF||$NiCoS_x$@$Ni_3S_2$/NF) was assembled to evaluate the OWS performance. The Faradaic efficiency (FE) of the overall water-splitting system was evaluated by a gas-collection (drainage) method. As shown in Fig. 6c, the measured $H_2/O_2$ volume ratio is close to the theoretical value of 2:1, indicating an FE approaching 100% and confirming that nearly all the input electrons are effectively utilized for water splitting, with negligible side reactions. To rigorously evaluate the catalytic performance, a commercial noble-metal-based electrolyzer using 20 wt% Pt/C/NF as the cathode and $RuO_2$/NF as the anode ($RuO_2$/NF||Pt/C/NF) was adopted as the benchmark for comparison. The $NiCoS_x$@$Ni_3S_2$/NF||$NiCoS_x$@$Ni_3S_2$/NF electrode exhibits an excellent OWS performance (1.54 V@10 mA $cm^{-2}$, 2.10 V@1000 mA $cm^{-2}$) comparable to that of Pt/C||$RuO_2$ (Fig. 6d, e), outperforming other reported catalysts (Fig. 6f, Table S4). The electrolyzer with $NiCoS_x$@$Ni_3S_2$/NF||$NiCoS_x$@$Ni_3S_2$/NF symmetric electrodes shows excellent long-term stability at varied constant potentials. At 1.62, 1.79, and 1.96 V, the initial current densities are 50.3, 99.3, and 498.4 mA $cm^{-2}$, with current retention of 95.6%, 94.1%, and 93.2%, respectively. The current density increases nearly tenfold with rising potential, realizing a superior activity-stability balance for practical applications (Fig. S39).

The protective role of the low-crystalline $NiCoS_x$ shell against sulfide leaching during OER was quantitatively assessed by ICP-OES analysis of the sulfur content before and after 192 h of continuous electrolysis at varying current densities (Tables S5–S7, Fig. S40). $NiCoS_x$@$Ni_3S_2$/NF exhibits a relative sulfur loss of only 5.7%, markedly lower than the 18.5% observed for bare $Ni_3S_2$/NF at 10 mA $cm^{-2}$. The core–shell architecture retains the majority of its sulfur content, with a loss of 9.6% at 100 mA $cm^{-2}$, whereas $Ni_3S_2$/NF suffers a 23.9% decrease. Under an industrially relevant load of 500 mA $cm^{-2}$, $NiCoS_x$@$Ni_3S_2$/NF displays a sulfur loss of 11.8%, in sharp contrast to the 27.5% loss recorded for $Ni_3S_2$/NF.

During the 192 h OER durability tests conducted at varying current densities (10, 100, and 500 mA $cm^{-2}$), the post-mortem ICP-MS analysis of electrolyte leaching concentrations and simultaneous monitoring of activity loss rates (Fig. S41) reveals a striking contrast in stability between $NiCoS_x$@$Ni_3S_2$/NF and $Ni_3S_2$/NF. $NiCoS_x$@$Ni_3S_2$/NF exhibited exceptional resistance to elemental leaching: under the harsh condition of 500 mA $cm^{-2}$, the leaching concentrations of Ni and Co remain < 1 ppm, S leaching reaches only 2 ppm, and the corresponding activity loss rate is strictly controlled below 5%. This ultra-stable performance originates from the Ni–Co–S heterostructural synergy, which enhances metal-sulfur (M–S) bond energy, suppresses the oxidation of $S^{2-}$ to $SO_4^{2-}$, and minimizes the formation of inert surface hydroxides, thereby preserving the integrity of active sites and the electronic structure of the M–S system. In stark contrast, the Co-free $Ni_3S_2$/NF, which possesses weaker M–S bond stability, exhibits significant leaching at 500 mA $cm^{-2}$, with Ni and S concentrations rising to 3 and 8.5 ppm, respectively, and the activity loss rate increase sharply to 35%. These findings confirm that Co doping and the construction of the Ni–Co–S heterostructure effectively

 https://doi.org/10.1007/s40820-026-02151-6

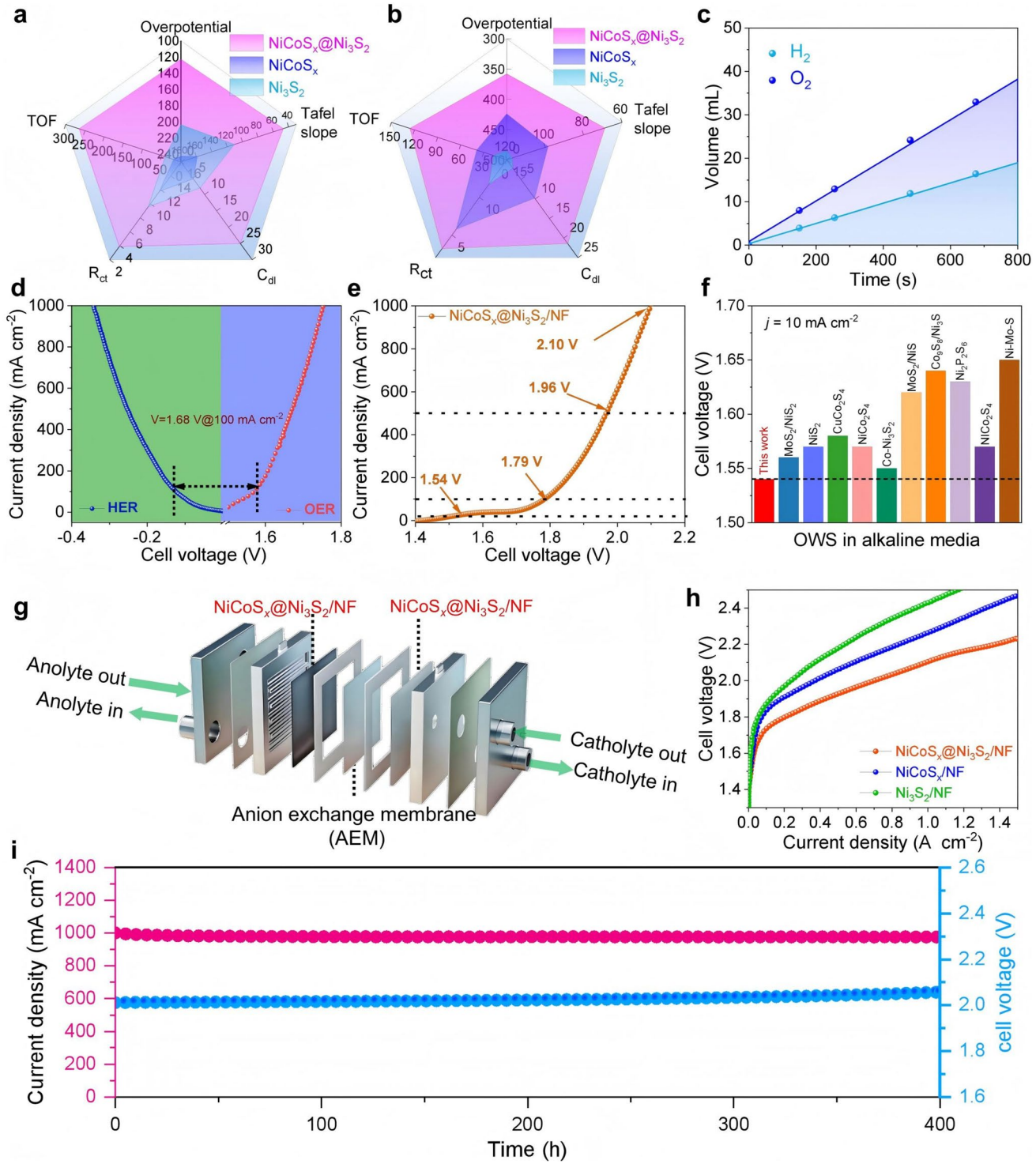


**Fig. 6** **a** HER and **b** OER performance of $Ni_3S_2$/NF, $NiCoS_x$/NF and $NiCoS_x@Ni_3S_2$/NF. **c** Volume of produced $H_2$ and $O_2$ as a function of time in a $NiCoS_x@Ni_3S_2$/NF electrolyzer. **d** HER and OER LSV polarization curves of $NiCoS_x@Ni_3S_2$/NF. **e** LSV polarization curves of $NiCoS_x@Ni_3S_2$/NF||$NiCoS_x@Ni_3S_2$/NF for OWS. **f** Comparison of OWS performance among the reported electrocatalysts. **g** Schematic diagram of the electrolyzer. **h** Polarization curves of the electrolyzer. **i** Current density and cell voltage curves of the electrolyzer during a 400 h stability test of $NiCoS_x@Ni_3S_2$/NF||$NiCoS_x@Ni_3S_2$/NF via long-term chronoamperometry/chronopotentiometry

buffer interfacial oxidation stress, inhibit elemental leaching and surface reconstruction, and thus are responsible for the ultra-high activity and stability of $NiCoS_x$@$Ni_3S_2$/NF even under high-current operating conditions.

To highlight the industrial application of anion exchange membrane water electrolysis (AEMWE) for hydrogen production, this study integrates a bifunctional electrode based on the core–shell structure $NiCoS_x$@$Ni_3S_2$/NF into an electrolyzer (Fig. 6g). Polarization curves show that the electrode exhibits excellent catalytic activity in both the anode OER and the cathode HER. It achieves a high current density of 1.0 A $cm^{-2}$ at a low overpotential of 2.12 V, demonstrating outstanding performance (Fig. 6h). Regarding stability, the electrode operates stability for 192 h, and even continuously for 400 h, showcasing the exceptional electrochemical durability provided by the core–shell structure (Fig. 6i).

More significantly, the nanorod morphology is essentially preserved after the OER reaction, with the formation of hydroxyl oxides on their surfaces (Fig. S42). XPS analysis reveals significant changes in the surface chemical states of the catalyst after HER and OER reactions: the appearance of a new peak in the Ni 2*p* and Co 2*p* spectrum after OER confirms the formation of NiOOH and CoOOH species; the Co 2*p* spectrum shows a 0.3 eV positive shift, indicating oxidation of Co species; In the S 2*p* spectrum, the intensity decreases after HER considering sulfur reduction/leaching, while peak broadening appears after OER attributing to sulfate formation. These results collectively reveal the dynamic evolution of the catalyst surface during the electrochemical reactions and their crucial impact on catalytic activity (Figs. S43, S44). This research provides a novel strategy for the development of efficient and stable industrial water electrolysis hydrogen production systems. Overall, the $NiCoS_x$@$Ni_3S_2$/NF bifunctional electrode demonstrates not only excellent catalytic activity and stability but also strong potential for industrial applications, making it a promising solution for constructing efficient, stable and scalable AEMWE hydrogen production systems.

To contextualize the durability of $NiCoS_x$@$Ni_3S_2$/NF, we systematically benchmarked its performance against recent state-of-the-art TMS electrocatalysts as summarized in Table S8. The survey shows that most reported sulfide-based OWS catalysts achieve long-term stability primarily at low-to-moderate current densities ($\leq 100 \sim 500$ mA $cm^{-2}$) for operation times ranging from several h to 200 h. Representative examples include $Co_9S_8$–$NiCo_2S_4$/N-rGO, which maintains negligible voltage growth for 15 h at $10 \sim 100$ mA $cm^{-2}$, and $NiCo_2S_4$@Ce-NiFe LDH/$CeO_2$ nanoarrays, which operate stably for 100 h at $50 \sim 100$ mA $cm^{-2}$. Only a few catalysts, such as $CeO_2$/$NiCo_2S_4$, demonstrate > 200 h durability at 500 mA $cm^{-2}$. In contrast, $NiCoS_x$@$Ni_3S_2$/NF exhibits continuous OWS operation for 192 h under stepwise current densities, reaching 1.0 A $cm^{-2}$ in 1.0 M KOH-approaching industrially relevant regimes while maintaining significantly higher sulfur retention compared with bare $Ni_3S_2$, as confirmed by ICP-OES analysis. The superior durability under harsher loads than most reported studies, results from the synergy of a low-crystalline $NiCoS_x$ shell, crystalline $Ni_3S_2$ core and a $\Delta\Phi$-induced BEF. These features collectively inhibit structural degradation and slow sulfur leaching during extended OER operation.

### 3.7 Density Functional Theory Calculation

Density functional theory (DFT) calculations were performed to gain deeper insights into the catalytic mechanism of $NiCoS_x$ and $Ni_3S_2$. Theoretical models of $Ni_3S_2$, $NiCoS_x$ and $NiCoS_x$@$Ni_3S_2$ were constructed and optimized (Fig. S45). The interfacial charge polarization revealed by charge density difference optimizes the intermediate adsorption at the heterostructure (Fig. S46a, b). To probe the interfacial charge dynamics in the heterostructure, the $\Delta\Phi$ for $Ni_3S_2$ (4.35 eV), $NiCoS_x$ (5.34 eV) and $NiCoS_x$@$Ni_3S_2$ (4.76 eV), reveals that BEF governs electron transfer across the heterogeneous interface (Fig. 7a). These values indicate that the heterogeneous interface layer gives rise to an asymmetric charge distribution generated by the BEF results. This BEF facilitates the easy transfer of electrons from electron-rich $NiCoS_x$ to electron-deficient $Ni_3S_2$, until the entire heterogeneous interface reaches a charge balance. This result is consistent with that of the UPS analysis (Fig. 1k).

Notably, the electron-rich $Ni_3S_2$ surface enhances H*/$H_2O$ adsorption, and the electron-deficient $NiCoS_x$ interface lowers the Gibbs free barrier for H*/*OH intermediate conversion. This synergistic electronic modulation optimizes the HER/OER kinetics, significantly boosting catalytic OWS performance. Molecular orbital theory elucidates the electronic coupling effects of Ni, S, and Co species in the $NiCoS_x$@$Ni_3S_2$/NF heterostructure, revealing an enhanced electron transfer mechanism that leads to its

 https://doi.org/10.1007/s40820-026-02151-6

superior catalytic performance. The low-spin state configuration ($t_{2g}^6e_{2g}^2$) of $Ni^{2+}$ indicates complete occupation of the π-symmetric d-orbitals, resulting in significant electron–electron (e-e) repulsion between the bridging $Ni^{2+}$ and $S^{2-}$ species. Conversely, $Co^{2+}$ exhibits a high-spin state configuration ($t_{2g}^3e_g^4$), characterized by unpaired electrons in the π-symmetric d-orbitals, facilitating electronic interactions with $S^{2-}$ through bridging coordination (Fig. S47a). Therefore, the chemical bonding between $NiCoS_x$ and $Ni_3S_2$ at the Ni–S–Co interface intensifies the electron–electron repulsion between $Co^{2+}$ and $S^{2-}$ species, thereby facilitating the formation of an extended π-electron cloud bridge between $Ni^{2+}$ and $S^{2-}$ species. This dynamic process contributes to the formation of Ni–S–Co by the electron coupling effect between $Co^{2+}$, $S^{2-}$, and $Ni^{2+}$, realizing the electron transfer from $NiCoS_x$ to $Ni_3S_2$ (Fig. S47b). Density of states (DOS) analysis was performed on $Ni_3S_2$, $NiCoS_x$ and $NiCoS_x@Ni_3S_2$ models to elucidate their catalytic mechanism. The DOS near the $E_f$ of the $NiCoS_x@Ni_3S_2$ is primarily contributed by the 3*d* orbitals of Co and Ni, rather than the 2*p* orbital of sulfur, suggesting that the adsorption behavior of reaction intermediates on the catalyst surface is predominantly governed by the electronic interaction mechanism between Co atoms and Ni atoms. As shown in the Fig. 7b, the d-band centers of Ni/Co active sites (− 1.67/− 1.44 eV) in the $NiCoS_x@Ni_3S_2$ are in between those of $Ni_3S_2$ (− 1.78 eV) and $NiCoS_x$ (− 1.29 eV), indicating that the adsorption energy of HER/OER intermediates in $NiCoS_x@Ni_3S_2$ is neither too strong nor too weak, thereby enhancing the electrocatalytic activity (Fig. 7c).

To explore the regulation mechanism of catalyst composition, interface microstructure and active site configuration on the kinetics of the HER, this study systematically characterizes the free energy evolution of $Ni_3S_2$, $NiCoS_x$ and $NiCoS_x@Ni_3S_2$ (Co and Ni active sites) in the HER process based on first-principles calculations. The results show that $Ni_3S_2$ mainly catalyzes HER via the Volmer-Heyrovsky pathway, with a high rate-determining step (RDS) barrier of 0.92 eV (Fig. 7d). Co doping improves the catalytic activity of $NiCoS_x$ by rearranging the electronic structure and adjusting hydrogen adsorption energy, lowering the RDS barrier to 0.87 eV (Fig. 7e). In the $NiCoS_x@Ni_3S_2$ heterojunction, Co doping induces electronic coupling and synergistic effects, reducing the RDS barrier further to 0.61 eV at the Co site and 0.53 eV at the Ni site (Fig. 7f, g). This shifts the HER reaction to follow the Volmer-Tafel pathway, demonstrating excellent intrinsic activity. These results demonstrate that the synergistic strategy of heterostructure construction and Co doping effectively overcomes performance bottlenecks in sulfide-based catalysts, with Ni sites in the $NiCoS_x@Ni_3S_2$ heterojunction serving as high-activity centers.

The OER in KOH electrolyte involves a four-electron "energy-climbing" process, and the activity is closely related to the magnitude of the Gibbs free energy (ΔG) of the intermediates on the material surface. This study constructed seven DFT models, including $Ni_3S_2$, $Ni_3S_2$/NiOOH, $NiCoS_x$/NiOOH, $NiCoS_x$/CoOOH, $NiCoS_x@Ni_3S_2$, $NiCoS_x@Ni_3S_2$/NiOOH, $NiCoS_x@Ni_3S_2$/CoOOH (Fig. S45) to explore the regulatory mechanism of interface reconstruction on catalytic kinetics. DFT free energy calculations reveal a stepwise optimization mechanism for OER kinetics driven by heterojunction interface reconstruction: $Ni_3S_2$ exhibits strong adsorption of *OH/*O intermediates due to the low electronegativity of sulfur atoms, resulting in a high energy barrier of 3.37 eV ($\Delta G_3$) for the RDS OH → O step (Fig. S48a). In contrast, the $NiCoS_x$/NiOOH heterojunction lowers the energy barrier to 2.39 eV ($\Delta G_2$), due to the coupling of the interface S–O bond and the oxygen-evolving properties of NiOOH, confirming the crucial role of the reconstructed layer (Fig. S48b, c). Upon further cobalt doping, the high-spin state of $Co^{3+}$ ($t_{2g}^3e_g^4$) in $NiCoS_x@Ni_3S_2$/NiOOH optimizes the OOH adsorption configuration, lowering the rate-determining O → *OOH energy barrier to 2.09 eV, lower than that at the Ni site (2.28 eV). This advantage stems from the defect-rich low-crystallinity $NiCoS_x$ layer (ECSA = 25.1 mF $cm^{-2}$) and BEF-driven charge transfer ($R_{st}$ = 3.1 Ω). Ultimately, the theoretical energy barrier aligns closely with the experimental overpotential (229 mV@10 mA $cm^{-2}$), confirming that the pre-reconstructed sulfide interface continuously enhances the kinetics of the reconstructed layer through electronic coupling.

To explore the catalytic dynamics of the catalyst in the OER, this study uses first-principles calculations to compare the free energy evolution paths of the AEM and the LOM. The results show that the OER reaction primarily follows the LOM path, with a significantly lower energy barrier compared to the AEM path. In the AEM path, the RDS energy barriers for Ni and Co sites are 2.14 and 2.28 eV, respectively (Fig. 7h). In the LOM path, the energy barrier for the O site is the lowest at 1.89 eV, with 2.11 and 2.43 eV for the Ni and Co sites, respectively (Fig. 7i). This indicates that LOM is the dominant reaction pathway, with the O site

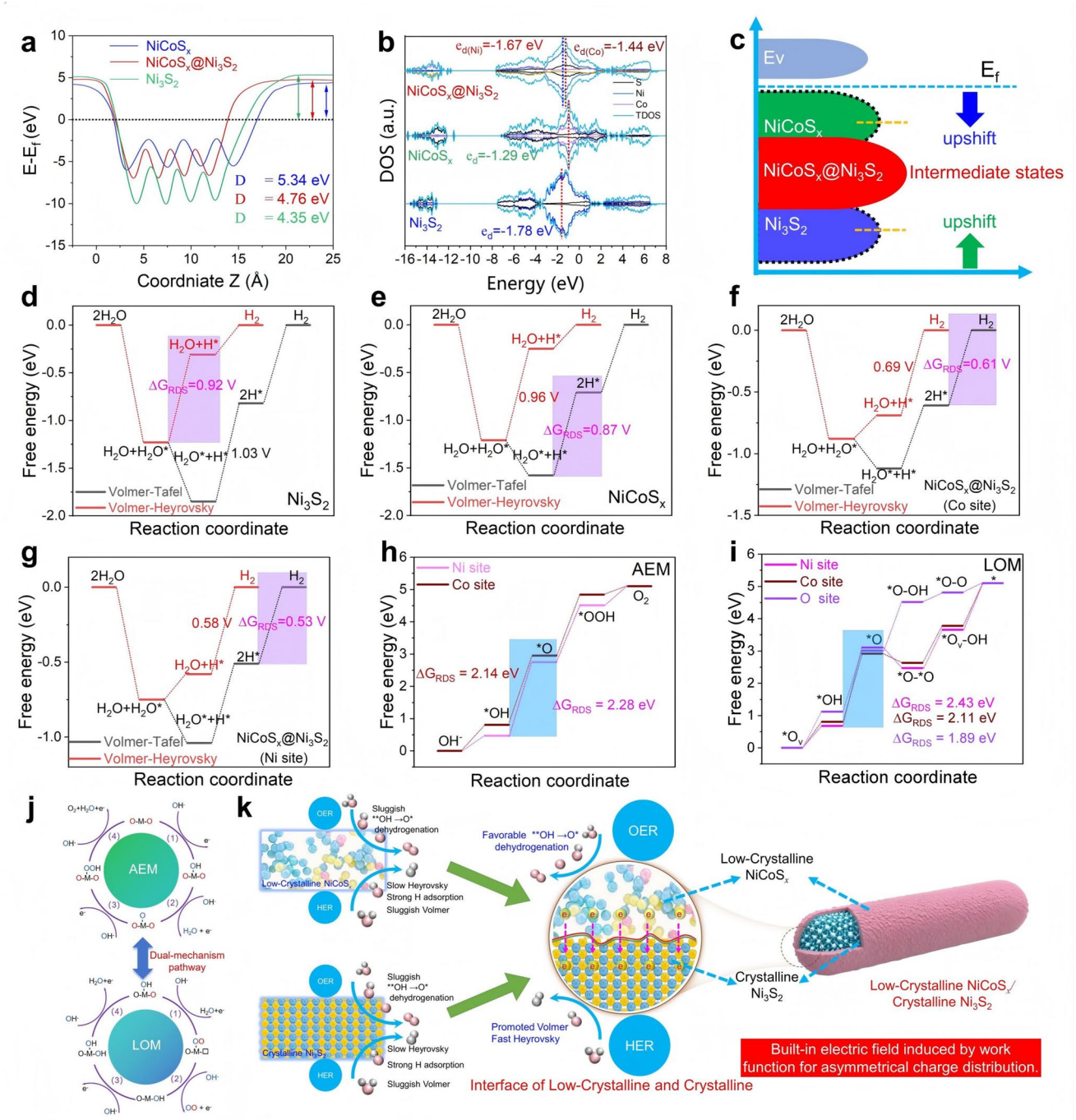


**Fig. 7** The mechanism of simulation calculation. **a** ΔΦ of the $Ni_3S_2$, $NiCoS_x$, and $NiCoS_x$@$Ni_3S_2$. **b** DOSs and **c** schematic diagram of d-band center of $Ni_3S_2$, $NiCoS_x$, and $NiCoS_x$@$Ni_3S_2$. Free energy profiles of hydrogen evolution reaction via Volmer-Tafel and Volmer-Heyrovsky pathways on: **d** $Ni_3S_2$, **e** $NiCoS_x$, **f** $NiCoS_x$@$Ni_3S_2$ Ni site, and **g** $NiCoS_x$@$Ni_3S_2$ Co site. Free energy profiles of the OER via the **h** AEM mechanism and **i** LOM mechanism. **j** Schematic illustration of the dual-mechanism pathways AEM and LOM for oxygen evolution reaction. **k** Schematic illustration of the catalytic mechanism for the enhanced OER and HER at the $NiCoS_x$@$Ni_3S_2$ heterointerface

playing a key role in the LOM path (Fig. 7j). These findings provide theoretical support for designing efficient OER catalysts by regulating the participation of lattice oxygen.

The enhanced HER and OER activities of the $NiCoS_x$@$Ni_3S_2$/NF catalyst originate from the spontaneous electron transfer induced by the work function difference (ΔΦ) at


https://doi.org/10.1007/s40820-026-02151-6

the $NiCoS_x/Ni_3S_2$ interface, which generates a robust BEF with asymmetric charge distribution (Fig. 7k). This BEF significantly optimizes reaction kinetics: (1) For HER, it lowers the energy barrier for water dissociation (Volmer step: $H_2O \rightarrow H^* + OH^-$) and facilitates hydrogen adsorption/desorption (Heyrovsky step). Specifically, H* preferentially adsorbs on the negatively charged $Ni_3S_2$ side, where it combines with another H* and electrons to form $H_2$. (2) For OER, the BEF reduces the activation energy for O–O bond formation and accelerates the RDS (*OH → *O) by stabilizing intermediates on the positively charged $NiCoS_x$. Therefore, the crystalline $Ni_3S_2$ nanorods tuned by low-crystalline $NiCoS_x$ with BEF enable superior dual functionality for efficient overall water splitting.

## 4 Conclusions

In summary, we synthesize a novel electrocatalyst of $NiCoS_x@Ni_3S_2$ by making use of low-crystalline $NiCoS_x$ to tune crystalline $Ni_3S_2$ nanorods via ion-exchange strategy, where the low-crystalline $NiCoS_x$ shell endows the catalyst with multiple synergistic advantages: enriched active sites from atomic disorder, optimized electron transfer from the built-in electric field induced by work function difference, dynamic surface reconstruction into high-activity NiCoOOH, and enhanced structural stability via suppressing sulfide leaching. The optimized $NiCoS_x@Ni_3S_2$ achieves low HER/OER overpotentials of 346/520 mV@1000 mA $cm^{-2}$, evidenced by an ultralow cell voltage of 2.10 V@1000 mA $cm^{-2}$ for OWS and remarkable long-term stability for 400 h at various current densities. Based on in situ Raman, XPS and DFT simulations, the superior catalytic performance and exceptional stability are ascribed to the following factors: (**i**) The inner layer is high crystalline $Ni_3S_2$, exhibiting exceptional electrical conductivity, while the outer surface layer is composed of low-crystalline $NiCoS_x$ with abundant defect sites; (**ii**) The BEF in $NiCoS_x@Ni_3S_2$ accelerates water dissociation, optimizes hydrogen adsorption/desorption for HER, and reduces the reaction energy barrier of *O → *OOH for OER, thereby promoting the overall catalytic kinetics of water splitting; (**iii**) The low-crystalline $NiCoS_x$ layer with the strong Ni–S–Co interfacial bridge acts an armor to suppress the sulfide loss, resulting in high catalytic activity and stability. This work paves a way to fabricate sulfur-based electrocatalysts with high yet balanced activity and stability for OWS via interface engineering strategy.

**Acknowledgements** This work was funded by the National Natural Science Foundation of China (Nos. 52372037 and 22108003), the Outstanding Scientific Research and Innovation Team Program of Higher Education Institutions of Anhui Province (No. 2023AH010015), the China Postdoctoral Science Foundation (No. 2024M750012), and the Excellent Young Talents Fund Program of Higher Education Institutions of Anhui Province (No. 2023AH030026). The authors appreciate the financial support from the Anhui International Research Center of Energy Materials Green Manufacturing and Biotechnology.

**Author Contributions** Huan Pang, Jieshan Qiu, and Xiaojun He supervised the project and conceived the idea. Neng Chen synthesized the materials, carried out the electrochemical tests, and performed all data analysis with visualization. Haoran Qian and Dedong Jia provided the DFT calculations for this work. Jun He, Hongqiang Li and Yongfeng Li assisted in the experimental tests and result analyses. All authors contributed to discussion of the results and have approved the final version of the manuscript.

**Declarations**

**Conflict of interest** The authors declare no interest conflict. They have no known competing financial interests or personal relationships that could have appeared to influence the work reported in this paper.



**Supplementary Information** The online version contains supplementary material available at https://doi.org/10.1007/s40820-026-02151-6.

## References

1. B. You, Y. Sun, Innovative strategies for electrocatalytic water splitting. Acc. Chem. Res. **51**(7), 1571–1580 (2018). https://doi.org/10.1021/acs.accounts.8b00002

2. Y. Luo, Z. Zhang, M. Chhowalla, B. Liu, Recent advances in design of electrocatalysts for high-current-density water splitting. Adv. Mater. **34**(16), e2108133 (2022). https://doi.org/10.1002/adma.202108133
3. Q. Hu, K. Gao, X. Wang, H. Zheng, J. Cao et al., Subnanometric Ru clusters with upshifted D band center improve performance for alkaline hydrogen evolution reaction. Nat. Commun. **13**(1), 3958 (2022). https://doi.org/10.1038/s41467-022-31660-2
4. C. Zhang, Z. Xu, N. Han, Y. Tian, T. Kallio et al., Superaerophilic/superaerophobic cooperative electrode for efficient hydrogen evolution reaction *via* enhanced mass transfer. Sci. Adv. **9**(3), eadd6978 (2023). https://doi.org/10.1126/sciadv.add6978
5. X. Gao, Y. Chen, Y. Wang, L. Zhao, X. Zhao et al., Next-generation green hydrogen: progress and perspective from electricity, catalyst to electrolyte in electrocatalytic water splitting. Nano-Micro Lett. **16**(1), 237 (2024). https://doi.org/10.1007/s40820-024-01424-2
6. C.-T. Hsieh, X.-F. Chuah, C.-L. Huang, H.-W. Lin, Y.-A. Chen et al., NiFe/(Ni, Fe)$_3$S$_2$ core/shell nanowire arrays as outstanding catalysts for electrolytic water splitting at high current densities. Small Methods **3**(10), 1900234 (2019). https://doi.org/10.1002/smtd.201900234
7. J. Thakur, P. Phogat, Shreya, Catalyst design for efficient water splitting: a comprehensive review of challenges and opportunities. Fuel **392**, 134954 (2025). https://doi.org/10.1016/j.fuel.2025.134954
8. Z. Shi, Z. Niu, W. Guo, Y. Leng, Y. Chen et al., Tip-encapsulated FeNi$_3$ in wood-derived N-doped CNTs arrays for efficient and stable AEM seawater electrolysis. Adv. Mater. **38**(3), e13754 (2026). https://doi.org/10.1002/adma.202513754
9. Y.-Q. Wang, H.-B. Zhao, J.-B. Cheng, B.-W. Liu, Q. Fu et al., Hierarchical $Ti_3C_2T_x$@ZnO hollow spheres with excellent microwave absorption inspired by the visual phenomenon of eyeless urchins. Nano-Micro Lett. **14**(1), 76 (2022). https://doi.org/10.1007/s40820-022-00817-5
10. Q. Shi, C. Zhu, D. Du, Y. Lin, Robust noble metal-based electrocatalysts for oxygen evolution reaction. Chem. Soc. Rev. **48**(12), 3181–3192 (2019). https://doi.org/10.1039/c8cs00671g
11. A.H. Shah, Z. Zhang, Z. Huang, S. Wang, G. Zhong et al., The role of alkali metal cations and platinum-surface hydroxyl in the alkaline hydrogen evolution reaction. Nat. Catal. **5**(10), 923–933 (2022). https://doi.org/10.1038/s41929-022-00851-x
12. F. Hu, D. Yu, M. Ye, H. Wang, Y. Hao et al., Lattice-matching formed mesoporous transition metal oxide heterostructures advance water splitting by active Fe–O–Cu bridges. Adv. Energy Mater. **12**(19), 2200067 (2022). https://doi.org/10.1002/aenm.202200067
13. H. Zhang, A.W. Maijenburg, X. Li, S.L. Schweizer, R.B. Wehrspohn, Bifunctional heterostructured transition metal phosphides for efficient electrochemical water splitting. Adv. Funct. Mater. **30**(34), 2003261 (2020). https://doi.org/10.1002/adfm.202003261
14. S. Liu, Y. Wei, M. Wang, Y. Shen, The future of alkaline water splitting from the perspective of electrocatalysts-seizing today's opportunities. Coord. Chem. Rev. **522**, 216190 (2025). https://doi.org/10.1016/j.ccr.2024.216190
15. H. Wang, J. Li, K. Li, Y. Lin, J. Chen et al., Transition metal nitrides for electrochemical energy applications. Chem. Soc. Rev. **50**(2), 1354–1390 (2021). https://doi.org/10.1039/d0cs00415d
16. H. Du, S. He, B. Li, K. Wang, Z. Zhou et al., Cascade reaction enables heterointerfaces-enriched nanoarrays for ampere-level hydrogen production. Angew. Chem. Int. Ed. **64**(12), e202422393 (2025). https://doi.org/10.1002/anie.202422393
17. H. Su, S. Song, S. Li, Y. Gao, L. Ge et al., High-valent bimetal $Ni_3S_2/Co_3S_4$ induced by Cu doping for bifunctional electrocatalytic water splitting. Appl. Catal. B Environ. **293**, 120225 (2021). https://doi.org/10.1016/j.apcatb.2021.120225
18. Y. Zhang, H. Li, X. Liu, Z.X. Hui, Z.W. Chen et al., Sub-3 nm high-entropy alloy nanoparticles with triple functionalities for efficient electrolytic hydrogen production. Adv. Mater. **37**(42), e08975 (2025). https://doi.org/10.1002/adma.202508975
19. W.-G. Cui, F. Gao, G. Na, X. Wang, Z. Li et al., Insights into the pH effect on hydrogen electrocatalysis. Chem. Soc. Rev. **53**(20), 10253–10311 (2024). https://doi.org/10.1039/d4cs00370e
20. W. Chen, W. Wei, F. Li, Y. Wang, M. Liu et al., Tunable built-in electric field in Ru nanoclusters-based electrocatalyst boosts water splitting and simulated seawater electrolysis. Adv. Funct. Mater. **34**(7), 2310690 (2024). https://doi.org/10.1002/adfm.202310690
21. Q. Quan, Y. Zhang, F. Wang, X. Bu, W. Wang et al., Topochemical domain engineering to construct 2D mosaic heterostructure with internal electric field for high-performance overall water splitting. Nano Energy **101**, 107566 (2022). https://doi.org/10.1016/j.nanoen.2022.107566
22. X. Wang, Z. Zhang, H. Zhang, S. Lin, C. Li et al., Crystalline/amorphous phosphide heterostructures with built-in electric fields for efficient and long-term industrial-scale alkaline water electrolysis. Adv. Funct. Mater. **36**(5), e14137 (2026). https://doi.org/10.1002/adfm.202514137
23. P. Tian, W. Zong, J. Xiong, W. Liu, J. Liu et al., Dynamic reconstruction of crystal/amorphous hetero-phosphate Janus interfaces for highly stable seawater splitting. Adv. Funct. Mater. **35**(42), 2504862 (2025). https://doi.org/10.1002/adfm.202504862
24. F. Ikram, S. Cheong, I. Persson, Z.R. Ramadhan, A.R. Poerwoprajitno et al., Iridium nanocrystals enriched with defects and atomic steps to enhance oxygen evolution reaction performance. J. Am. Chem. Soc. **147**(12), 10784–10790 (2025). https://doi.org/10.1021/jacs.5c02151
25. X. Chen, J. Wang, Y. Chai, Z. Zhang, Y. Zhu, Efficient photocatalytic overall water splitting induced by the giant internal electric field of Ag-$C_3N_4$/rGO/PDIP Z-scheme heterojunction. Adv. Mater. **33**(7), e2007479 (2021). https://doi.org/10.1002/adma.202007479


 https://doi.org/10.1007/s40820-026-02151-6

26. Y.-J. Chen, J.-Z. Zhang, Z.-X. Wu, Y.-X. Qiao, L. Zheng et al., Molecular engineering of perylene diimide polymers with a robust built-in electric field for enhanced solar-driven water splitting. Angew. Chem. Int. Ed. **63**(8), e202318224 (2024). https://doi.org/10.1002/anie.202318224
27. S.S. Mali, J.V. Patil, J.-Y. Shao, Y.-W. Zhong, S.R. Rondiya et al., Phase-heterojunction all-inorganic perovskite solar cells surpassing 21.5% efficiency. Nat. Energy **8**(9), 989–1001 (2023). https://doi.org/10.1038/s41560-023-01310-y
28. Y. Gao, Q. Zhang, W. Hu, J. Yang, First-principles computational screening of two-dimensional polar materials for photocatalytic water splitting. ACS Nano **18**(29), 19381–19390 (2024). https://doi.org/10.1021/acsnano.4c06544
29. H. Lan, J. Wang, L. Cheng, D. Yu, H. Wang et al., The synthesis and application of crystalline–amorphous hybrid materials. Chem. Soc. Rev. **53**(2), 684–713 (2024). https://doi.org/10.1039/d3cs00860f
30. Z. Wang, S. Wang, Constructing built-in electric field to accelerate the asymmetric local charge distribution for efficient alkaline overall water/seawater splitting. Appl. Catal. B Environ. Energy **352**, 124002 (2024). https://doi.org/10.1016/j.apcatb.2024.124002
31. W. Zhang, L. Yang, Z. Li, G. Nie, X. Cao et al., Regulating hydrogen/oxygen species adsorption *via* built-in electric field-driven electron transfer behavior at the heterointerface for efficient water splitting. Angew. Chem. Int. Ed. **63**(16), e202400888 (2024). https://doi.org/10.1002/anie.202400888
32. Y. Zhang, F. Gao, D. Wang, Z. Li, X. Wang et al., Amorphous/crystalline heterostructure transition-metal-based catalysts for high-performance water splitting. Coord. Chem. Rev. **475**, 214916 (2023). https://doi.org/10.1016/j.ccr.2022.214916
33. X. Xu, L. Meng, J. Zhang, S. Yang, C. Sun et al., Full-spectrum responsive naphthalimide/perylene diimide with a giant internal electric field for photocatalytic overall water splitting. Angew. Chem. Int. Ed. **63**(5), e202308597 (2024). https://doi.org/10.1002/anie.202308597
34. Q. Zhou, Y. Guo, Z. Ye, Y. Fu, Y. Guo et al., Carbon nitride photocatalyst with internal electric field induced photogenerated carriers spatial enrichment for enhanced photocatalytic water splitting. Mater. Today **58**, 100–109 (2022). https://doi.org/10.1016/j.mattod.2022.06.009
35. S. Zhang, C. Tan, R. Yan, X. Zou, F.-L. Hu et al., Constructing built-in electric field in heterogeneous nanowire arrays for efficient overall water electrolysis. Angew. Chem. Int. Ed. **62**(26), e202302795 (2023). https://doi.org/10.1002/anie.202302795
36. H. Zhang, N. Li, S. Gao, A. Chen, Q. Qian et al., Quenching-induced atom-stepped bimetallic sulfide heterointerface catalysts for industrial hydrogen generation. eScience **5**(2), 100311 (2025). https://doi.org/10.1016/j.esci.2024.100311
37. C. Pei, S. Chen, J. Xie, S. Feng, M. Yu et al., Strain engineering in gradient-structured metallic glasses for excellent overall water splitting. Mater. Today **85**, 100–111 (2025). https://doi.org/10.1016/j.mattod.2025.02.024
38. Y. Wang, X. Li, Z. Huang, H. Wang, Z. Chen et al., Amorphous Mo-doped $NiS_{0.5}Se_{0.5}$ nanosheets@crystalline $NiS_{0.5}Se_{0.5}$ nanorods for high current-density electrocatalytic water splitting in neutral media. Angew. Chem. Int. Ed. **62**(6), e202215256 (2023). https://doi.org/10.1002/anie.202215256
39. K. Song, H. Liu, B. Chen, C. Gong, J. Ding et al., Toward efficient utilization of photogenerated charge carriers in photoelectrochemical systems: engineering strategies from the atomic level to configuration. Chem. Rev. **124**(24), 13660–13680 (2024). https://doi.org/10.1021/acs.chemrev.4c00382
40. B. Lu, R. Dun, W. Wang, J. Huang, J. Wu et al., Electroless plating synthesis of bifunctional crystalline/amorphous Pd-NiFeB heterostructure catalysts for boosted electrocatalytic water splitting. Appl. Catal. B Environ. **342**, 123343 (2024). https://doi.org/10.1016/j.apcatb.2023.123343
41. H. Sun, X. Xu, G. Chen, Z. Shao, Perovskite oxides as electrocatalysts for water electrolysis: from crystalline to amorphous. Carbon Energy **6**(11), e595 (2024). https://doi.org/10.1002/cey2.595
42. X. Li, Z. Xie, S. Roy, L. Gao, J. Liu et al., Amorphous high-entropy phosphide nanosheets with multi-atom catalytic sites for efficient oxygen evolution. Adv. Mater. **37**(10), 2410295 (2025). https://doi.org/10.1002/adma.202410295
43. D. Zha, R. Wang, S. Tian, Z.-J. Jiang, Z. Xu et al., Defect engineering and carbon supporting to achieve Ni-doped $CoP_3$ with high catalytic activities for overall water splitting. Nano-Micro Lett. **16**(1), 250 (2024). https://doi.org/10.1007/s40820-024-01471-9
44. Y. Wang, H. Qin, X. Wang, F. Yan, Y. Zhao et al., Interface-engineered construction of amorphous FeNi(OH) X and crystalline Ni3S2 heterojunction catalysts for achieving efficient bifunctional electrocatalysts in overall water splitting. Chemsuschem **18**(19), e202501240 (2025). https://doi.org/10.1002/cssc.202501240
45. M. Zheng, J. Du, B. Hou, C.-L. Xu, Few-layered $Mo_{(1-x)}W_xS_2$ hollow nanospheres on $Ni_3S_2$ nanorod heterostructure as robust electrocatalysts for overall water splitting. ACS Appl. Mater. Interfaces **9**(31), 26066–26076 (2017). https://doi.org/10.1021/acsami.7b07465
46. H. Su, S. Song, Y. Gao, N. Li, Y. Fu et al., *In situ* electronic redistribution tuning of $NiCo_2S_4$ nanosheets for enhanced electrocatalysis. Adv. Funct. Mater. **32**(14), 2109731 (2022). https://doi.org/10.1002/adfm.202109731
47. P. Wang, Y. Luo, G. Zhang, Z. Chen, H. Ranganathan et al., Interface engineering of $Ni_xS_y$@$MnO_xH_y$ nanorods to efficiently enhance overall-water-splitting activity and stability. Nano-Micro Lett. **14**(1), 120 (2022). https://doi.org/10.1007/s40820-022-00860-2
48. S. Qiang, Z. Li, S. He, H. Zhou, Y. Zhang et al., Modulating electronic structure of $CoS_2$ nanorods by Fe doping for efficient electrocatalytic overall water splitting. Nano Energy **134**, 110564 (2025). https://doi.org/10.1016/j.nanoen.2024.110564
49. M. Wu, F. Dong, Y. Yang, X. Cui, X. Liu et al., Emerging atomically precise metal nanoclusters and ultrasmall

nanoparticles for efficient electrochemical energy catalysis: synthesis strategies and surface/interface engineering. Electrochem. Energy Rev. **7**(1), 10 (2024). https://doi.org/10.1007/s41918-024-00217-w

50. S.H. Kim, J.Y. Park, S.Y. Choi, J. Mo, H.-C. Song et al., Interface engineering of LaSrCoO-N-CDs-FeOOH composites for synergistic water-splitting catalysis. Nano Energy **142**, 111170 (2025). https://doi.org/10.1016/j.nanoen.2025.111170
51. Y. Wu, B. Xiao, K. Liu, S. Wang, Y. Hou et al., Electrochemical synthesis of high-efficiency water electrolysis catalysts. Electrochem. Energy Rev. **8**(1), 2 (2025). https://doi.org/10.1007/s41918-024-00237-6



 https://doi.org/10.1007/s40820-026-02151-6